M.Sci Thesis
Meteorology

Turbulent CO_2 exchange and surface energy balance over melting fjord-ice in North-East Greenland

Siiri Wickström

25. May 2015

Supervisor(s): Dos. Timo Vihma, Prof. Tim Papakyriakou

Reviewer(s): Prof. Timo Vesala, Dos. Timo Vihma

UNIVERSITY OF HELSINKI
DEPARTMENT OF PHYSICS

PL 64 (Gustaf Hällströmin katu 2)
00014 University of Helsinki

HELSINGIN YLIOPISTO — HELSINGFORS UNIVERSITET

Tiedekunta — Fakultet	Laitos — Institution
Matemaattis-luonnontieteellinen	Fysiikan laitos

Tekijä — Författare
Siiri Wickström

Työn nimi — Arbetets titel

Turbulent CO_2 exchange and surface energy balance over melting fjord-ice in North-East Greenland

Oppiaine — Läroämne
Meteorologia

Työn laji — Arbetets art	Aika — Datum	Sivumäärä — Sidoantal
Pro gradu -tutkielma	Kesäkuu 2015	60 s. + 2s. liitteet

Tiivistelmä — Referat

Tutkielmassa tarkastelen merijään ja ilmakehän välisen hiilidioksidinvaihdon yhteyttä sulavan merijääpinnan energiataseeseen. Tuoreet tutkimukset ovat osoittaneet että merijään sulaminen voi toimia merkittävänä hiilidioksidin nieluna Arktisilla merillä. Sulamisprosessin on esitetty laimentavan jään sekä pintaveden hiilidioksidin osapainetta (pCO_2), mikä voimistaisi meren alikyllästystä hiilidioksidin suhteen. Myös jäähän liittyvä biologia sekä jäänsisäinen karbonaattikemia muokkaavat ilmakehän, jään ja meren välistä CO_2-pitoisuuden gradienttia. Pienetkin vuot merijään lävitse voivat olla potentiaalisesti merkittäviä ottaen huomioon, että laajimmillaan merijää kattaa noin 7 prosenttia maapallon pinta-alasta. Monivuotisen Arktisen merijään vähentyessä muuttuvassa ilmastossa suurempi osuus merijääpeitteestä sulaa vuosittain ja sulamisprosessien vaikutus ilmastoomme on suurempi. Tämän hetkiset globaalit ilmasto- ja biogeokemiamallit käsittelevät merijäätä kaasuja läpäisemättömänä eristeenä ilmakehän ja napamerien välillä, minkä seurauksena hiilidioksidinkierron muutosten ennustaminen on puutteellista.
Energiatase muodostuu nettosäteilystä, turbulenttisista havaittavan lämmön ja latentin lämmön voista sekä jään läpi pintaan johtuvasta lämmöstä. Sulaessaan merijään pinta muuttuu tasaisesta lumipeitteestä sulavesilammikoiden peittämäksi. Sulavan pinnan heijastavuuden lasku kontrolloi energiatasetta, sillä suurempi osa auringonsäteilystä imeytyy pintaan ja voimistaa sulamista entisestään. Merijään lämpötilaan vaikuttavat ilmakehän, jään ja meren välinen energianvaihto sekä jään huokoisuus.
Tutkielma perustuu 30 päivän kenttämittauskampanjaan kesäkuussa 2014 Young Sound -vuonosta, Koillis-Grönlannista ($74°18^{'}N,\ 20°13^{'}W$). Turbulenttista hiilidioksidin ja vesihöyryn vuota mitattiin 10 Hz:n taajuudella kahdella avoimella (open-path) infrapunakaasuanalysaattorilla ja akustisella anemometrilla n. 3 m korkeudella. Ilmakehän perussuureita (tuuli, säteily, kosteus, lämpötila) mitattiin yhdellä mastolla. Pintaveden hiilidioksidipitoisuutta mitattiin jatkuvasti 2.5 m syvyydeltä. Mastojen läheisyydestä kairatuista jäänäytteistä määritettiin jään lämpötila ja lämmönvuo. Turbulenssiaineistosta määritettiin CO_2:n ja vesihöyryn vuot Eddy Covariance â menetelmällä, jossa vuo määritetään pystytuulen sekä tarkasteltavan kaasun pitoisuuden turbulenttisten vaihteluiden kovarianssista. Heikot tuulet laskivat hyvänlaatuisten mittausten määrää, aiheuttaen aukkoja aikasarjaan.
Mitattu hiilidioksidinvuo vaihteli 1.92 ja -3.2 μmol m^{-2} s^{-1} (positiiviset vuot suuntautuvat pinnasta ilmaan) välillä ja merijää oli mittauskampanjan ajan hiilidioksidin nettonielu. Jää oli läpäisevyyden kynnysarvoa lämpimämpi koko mittausjakson ajan ja lämpeni tasaisesti kampanjan edetessä. Pintaveden pCO_2 oli koko mittauskampanjan ajan ilmakehän CO_2 pitoisuutta matalampi ja pintaveden alikylläisyys kasvoi 50 μatm:sta 140 μatm: aan 10 päivässä (13. â− 23. kesäkuuta). Voimakkaasta alikyllästystilasta huolimatta hiilidioksidinvuo jäähän ei kasvanut aikasarjan loppua kohden. Mahdollinen selitys tälle on sulavesilammikoiden saavuttama tasapaino ilmakehän pCO_2:n kanssa. Suurimmat hiilidioksidin vuot jäähän mitattiin sulavesilammikoiden muodostuessa. Suuria positiivista voita (vuo$>$ 1 μmol m^{-2} s^{-1}) havaittiin kahdesti, 11. ja 18. kesäkuuta.
Yleisesti hiilidioksidinvuon ja pinnan energiavoiden välillä ei havaittu voimakkaita merkitseviä korrelaatioita. Hiilidioksidinvuon ja nettosäteilyn sekä tuulen nopeuden välillä oli kuitenkin heikko positiivinen korrelaatio. Heikkoja korrelaatioita selittävät luultavasti useat merijään huokoisuuteen ja CO_2 pitoisuuteen vaikuttavat tekijät joiden vaikutuksia toisistaan ei voida eritellä käytössä olleella aineistolla. Tutkielma tukee hypoteesia siitä, että sulaessaan merijää on hiilidioksidin nielu. Mittausten laatua voisi parantaa käyttämällä suljettua kaasuanalysaattoria avoimen sijasta. Menetelmänä Eddy Covariance on puutteistaan huolimatta tällä hetkellä kehittynein ja luotettavin tapa mitata ekosysteemiskaalan turbulenttista vuota.

Avainsanat — Nyckelord
hiilidioksidi, merijää, eddy covariance, turbulentinen vuo, pinnan energiatase, Grönlanti

Säilytyspaikka — Förvaringsställe
Kumpulan tiedekirjasto, Helsingin yliopisto

Muita tietoja — övriga uppgifter

University of Helsinki

Tiedekunta — Fakultet	Faculty
Faculty of Science	Physics

Author
Siiri Wickström

Title

Turbulent CO_2 exchange and surface energy balance over melting fjord-ice in North-East Greenland

Subject
Meteorology

Level	Date	Number of pages
Master's thesis	June 2015	60 + appendix(2 pages)

Abstract

This study aims to connect air-sea ice turbulent carbon dioxide (CO_2) exchange and the surface energy balance over melting fjord ice. Recent studies have shown that sea ice melt might act as a significant CO_2 sink in Arctic waters. Melt process have been suggested to dilute both brine and surface water partial pressures of carbon dioxide(pCO_2). Also biological activity and carbonate chemistry changes the air-ocean CO_2 concentration gradient. Even small fluxes might be potentially significant as the maximum sea ice extent covers approximately 7% of Earth's surface. As multi-year ice diminishes with the on-going climate change a bigger portion of the ice cover will experience melt in the summer season and thus the melt induced changes on the carbon cycling in the Arctic will have a greater effect.

Surface energy balance consists of net radiation, turbulent fluxes of latent and sensible heat and conductive heat flux. During melt the sea ice surface transforms from a dry snow cover to melt ponds. Surface melt leads to a decrease in the surface albedo controlling the surface energy balance. Sea ice temperature affects both air-ice-ocean energy exchange and the permeability of the ice.

My thesis is based on a 30 day measurement campaign in June 2014 from The Young Sound fjord, in North-East Greenland ($74°18'N,\ 20°13'W$). Turbulent fluxes of CO_2 and H_2O were measured with 10 Hz with two open-path infrared gas-analysers and two sonic anemometers at approximately 3 m height. One mast was used to measure basic meteorology (temperature, humidity, radiation, wind). Continuous measurements of surface water pCO_2 were made 2.5 m below the ice. Conductive heat flux was determined from ice cores. The turbulent fluxes were calculated with the Eddy Covariance-methodology. Weak winds decreased the number of good quality measurements and created gaps in the time series.

The measured CO_2 flux ranged between 1.92 ja -3.2 μmol m^{-2} s^{-1} (positive fluxes being efflux) and sea ice was a net sink during the campaign. Sea ice temperature rose steadily with time, being above the permeability threshold in all measurements. Surface water pCO_2 was lower than the atmospheric throughout the study and the under saturation grew from 50 μatm to 140 μatm in 10 days (13. to 23. June). Despite the strong pCO_2 difference indicating ocean sink the CO_2 absorption at the ice surface did not show an increase over time. A possible explanation for this is the equilibration of the air-melt pond pCO_2 gradient. The strongest CO_2 uptake was recorded as the melt ponds formed. Two strong efflux events (flux > 1 μmol m^{-2} s^{-1}) were recorded on June 11 and 18.

In general no strong correlations were found between the surface energy budget and the air-surface CO_2 exchange. However, the CO_2 flux has a weak positive correlation both with wind speed and net radiation. The weak correlations are probably explained by the co-existence of different processes simultaneously affecting the air-ice-ocean CO_2 gradients.

The results support the hypothesis of melting sea ice acting as a sink for atmospheric CO_2. The measurement quality could be improved by using a closed-path gas analyser. Despite the challenges Eddy Covariance is currently the state-of-art methodology for measuring ecosystem-scale turbulent exchange.

Keywords
carbon dioxide, sea ice, Turbulent flux, surface energy balance, eddy covariance, Greenland

Where deposited
Kumpula science library, University of Helsinki

Additional information

Contents

1 Introduction

Current estimates show that polar seas are an important sink region for atmospheric CO_2. The highest uptake rates per unit area are found in high-latitude North Atlantic (Takahashi et al., 2002, 2012). In Arctic waters gas exchange is affected by the presence of an ice cover large parts of the year. Arctic climate has changed at least twice as fast as the global average in recent decades (Blunden and Arndt, 2012) and the Arctic sea ice conditions have undergone rapid changes. Sea ice has been retreating in all Arctic seas during all seasons, with the strongest decline in summer/autumn (Cavalieri and Parkinson, 2012). Remote sensing data reveals a 50% decrease in sea ice coverage in summer and autumn months between 1979 and 2011 (Stammerjohn et al., 2012). The remaining sea ice is becoming younger and thinner and, thus, more prone to melt (Stammerjohn et al., 2012). Based on coupled model experiments Overland et al. (2011) estimates that the first ice free summer in the Arctic will take place in approximately 35 years, around 2050.

Sea ice creates unique atmospheric and oceanographic boundary conditions. It acts as a physical barrier between the air and the ocean, reducing exchange of both energy and matter. Air-ice-sea interactions form a complex web of thermal and mechanical processes of varying scales (Vihma et al., 2014). Sea ice cuts off wind induced mixing of surface waters and cuts off moisture and heat fluxes from the ocean efficiently. The high albedo of ice and, especially snow, compared to open water affects the surface energy balance at the surface and controls the light conditions under ice (Warren, 1982; Serreze and Barry, 2005a). In agreement with the observed sea ice retreat, an increase in summer and autumn temperatures and humidities have been observed in the lower atmosphere (Screen and Simmonds, 2010).

The overall impact of sea ice on the Arctic atmosphere-ocean CO_2 sink remains debated (Parmentier et al., 2013). Arctic shelf surface waters are characterised by low pCO_2 values during the open water season, arguing for an increase in carbon uptake with retreating sea ice (Bates and Mathis, 2009). Contrary to this Else et al. (2013) shows with a simple model that surface warming and related increased stratification will eventually reduce the CO_2 uptake in ice-free Arctic waters. Sea ice itself has been viewed as a passive lid for gas exchange - to date no climate nor biogeochemical model accounts for gas exchange through sea ice (Tison et al., 2002; Toggweiler et al., 2003).

However, an increasing number of studies report gas exchange at the air-ice interface and suggest sea ice having an active role in the Arctic carbon cycle (Rysgaard et al., 2009; Geilfus et al., 2013; Papakyriakou and Miller, 2011; Sørensen et al., 2014; Sievers et al., 2015). Pioneering studies from mid-seventies found sea ice to be permeable to gases, including CO_2, in temperatures above -7 °C,

translating to brine volumes exceeding 5% (Gosink et al., 1976). In line with this, recent in-situ studies have reported atmosphere-ice CO_2 fluxes over sea ice from both hemispheres during all seasons.

The observed fluxes cover a large size range (see Tables 8 and 9 in Appendix A for previous Eddy Covariance and chamber measurements). Flux studies have been conducted both with micrometeorological masts and chambers. In general EC fluxes seem to be at least one order of magnitude larger than chamber measurements. The highest spring time uptake rates on seasonal fast ice are reported by Papakyriakou and Miller (2011) with hourly uptake of -3 μmol m^{-2} s^{-1} in the Canadian Arctic. Sievers et al. (2015) reports similar size fluxes earlier in the season from fast ice in Young Sound. The smallest EC fluxes encompasing sea ice melt, -0.2 to -0.05 μmol m^{-2} s^{-1}, are reported in Zemmelink et al. (2006) from a multi-year ice flow in the Souther Ocean. The largest overall fluxes, with a maximum uptake of -27.95 μmol m^{-2} s^{-1}, are wintertime fluxes from a polynya region (Else et al., 2011). Large effluxes in the size range 1-3 μmol m^{-2} s^{-1} are reported in several studie (Papakyriakou and Miller, 2011; Sievers et al., 2015; Miller et al., 2011; Else et al., 2011).

Most of the to date conducted air-ice CO_2 flux measurements are spring and summer studies over first year fast ice (Table 8). Eddy Covariance fluxes in Semiletov et al. (2004); Papakyriakou and Miller (2011); Miller et al. (2011) capture the melt season in the Arctic and Zemmelink et al. (2006) in the Antarctic. Sørensen et al. (2014) and Sievers et al. (2015) present early spring (March/April) EC flux measurements from fjord environments in Greenland. All chamber measurements covers sea ice melt, except Geilfus et al. (2013) capturing fluxes over newly formed ice. Wintertime EC fluxes are presented in Else et al. (2011) and Miller et al. (2011) .

The conducted studies support a strong seasonality of the ice-atmosphere CO_2 flux - with freeze-up emissions and melt absorption. Springtime studies report sea ice uptake rates comparable to open-water fluxes (Papakyriakou and Miller, 2011; Sørensen et al., 2014; Sievers et al., 2015). However early spring studies also report efflux. A tank experience by Nomura et al. (2006) suggests that 0.8 % of the total inorganic carbon trapped in the ice is released to the atmosphere when it freezes. The flux is suggested to be very small in mid-winter, especially in the presence of a thick snow cover on the ice. The magnitude of melt related CO_2 uptake seems to over take the fall emissions, making sea ice a net sink for atmospheric CO_2.

Formation and melt of sea ice, as well as biogeochemistry within the ice, has been shown drive the flux by affecting the CO_2 partial pressure (pCO_2) of brine and surface waters (Rysgaard et al., 2009). Brine expands/contracts with rising/sinking ice temperatures, controlling the pCO_2 within the ice (Eicken et al., 2002). Melt water percolation and brine drainage further affects the under ice pCO_2 values (Rysgaard et al., 2007, 2012; Skogseth et al., 2004). Wintertime supersaturation conditions in the brine have been shown to promote precipitation of hydrated

calcium carbonate crystals, such as ikaite (Rysgaard et al., 2012, 2014). These carbonate salts are proposed to act as an alkalinity storage within the ice, lowering the brine and, eventually surface water, pCO_2 during melt. In the melt season the air-ice pCO_2 gradient is also altered by primary production within and under ice.

Sea ice surface conditions are shown to be a strong control of both the the CO_2 exchange and the ice surface energy balance (Nomura et al., 2010, 2013; Else et al., 2013; Geilfus et al., 2013; Else et al., 2014). Especially in the melt season the surface undergoes drastic changes - dry snow cover transforms to a melt pond covered surface. Melt ponds have been perceived as significant contributors in the air-ice carbon exchange Semiletov et al. (2004); Geilfus et al. (2014). The albedo change of the surface makes melt ponds also strong control of the surface energy budget over ice (Else et al., 2014).

In addition, open water fractions in the sea ice environment influence carbon exchange. Polynyas are known to promote ice formation as well as being hotspots for biological activity (Arrigo et al., 1999). Leads and polynyas are also windows for direct air-ocean exchange of heat, moisture and momentum. Else et al. (2013) reports polynya influenced CO_2 uptake of 1 to 2 orders higher magnitude compared to open water fluxes over wintertime sea ice.

Rapid changes in surface energy balance together with ice temperatures above the permeability threshold , makes melt season carbon exchange over sea ice interesting.A number of studies report melt season fluxes from both hemisphere (Geilfus et al., 2014; Papakyriakou and Miller, 2011; Miller et al., 2011; Semiletov et al., 2004; Zemmelink et al., 2006; Sievers et al., 2015; Delille et al., 2014). However, fully developed melt ponds are reported only by Geilfus et al. (2014); Papakyriakou and Miller (2011); Miller et al. (2011); Semiletov et al. (2004). These studies consists of both micrometeorological tower measurements (Eddy Covariance - method in Miller et al. (2011); Papakyriakou and Miller (2011); Semiletov et al. (2004)) and chamber measurements (Geilfus et al., 2014; Semiletov et al., 2004). These studies point out the challenge in collecting good quality flux data over sea ice, in harsh Arctic conditions, and underline the importance of careful post processing of the raw data in such low flux conditions with possibly high noise-to-signal ratios (Papakyriakou and Miller, 2011).

Adequate accounting for CO_2 cycling in the Arctic is a prerequisite for better predictability of the climate change . This requires inclusion of sea ice driven carbon exchange. Even a small net air-ice exchange is potentially significant when up-scaled over the total sea ice area (Rysgaard et al., 2009) - at its seasonal maximum, Arctic sea ice covers roughly 7 % of Earth's surface area. Sea ice retreat has a large potential for feedbacks on the carbon balance in Arctic waters (Parmentier et al., 2013). To our knowledge only one attempt to parametrize CO_2 exchange over sea ice has been published to date (Sørensen et al., 2014). Improvement and

development of parametrizations require further research on surface structure and energetics, parallel with air-ice CO_2 flux measurements.

The goal of this study is to connect ice-air CO_2 flux and the surface energy budget over melting seasonal sea ice. Focus is laid on the quality of the data and the assessment of the significance of the flux. We aim to present a high quality flux dataset and to discuss it from the atmospheric energy exchange point of view.

Despite the growing number of conducted studies, no melt season flux measurements from the high latitude Northern Atlantic, a potential hotspot of CO_2 uptake, are reported. Here we presents spring and early summer measurements of turbulent CO_2 fluxes and surface energy balance components over land-fast first year fjord ice in Young Sound, North-East Greenland. The fjord system is connected to The Greenland Sea (see figure 4 for map). In addition to atmospheric measurements, surface water pCO_2 data and ice core data is utilized. Sea ice surface evolution was followed from late May to early July 2014 capturing the surface transformation from a 60 cm snow cover to melt ponds. The measurements were carried out as a part of the *Young Sound 2014* campaign organized by the *Arctic Partnership* consortia at the Daneborg research station run by Aarhus University, Denmark.

This work is divided into 6 chapters. In Chapter 2 the theoretical framework of sea ice related carbon exchange is presented. The study-set up, data collection and data processing is described in Chapter 3. The results are presented and discussed in Chapters 4 and 5 respectively. And finally, Chapter 6 brings the work to a conclusion, followed by the acknowledgements.

2 Theory

The first part of this chapter describes the role of sea ice in the Arctic climate system followed by a section dedicated to carbon cycling in the Arctic, focusing on the impact of sea ice on carbon dioxide exchange. The last section of this chapter presents turbulent flux calculation theory.

2.1 Sea ice in the Arctic climate system

The unique conditions in the Polar Regions are directly or indirectly a result of the low incoming solar energy, compared to equatorial regions. This allows year-round co-existence of all three forms of water. The perennial cryosphere consists of both sea ice and land ice, glaciers and permafrost (Serreze and Barry, 2005b). Perennial sea ice is found only in the Arctic and the Antarctic.

Sea ice is a relatively sensitive component of the climate system, experiencing both atmospheric and oceanic forcing. In addition to the low temperatures, relatively fresh surface waters with a higher freezing point are important for sea ice formation. River discharge, inflow of low salinity waters from the Bering Strait and precipitation, in relative order of importance, maintain fresh surface water conditions in the Arctic (Serreze and Barry, 2005c). This creates a pycnocline, a salinity induced density gradient, suppressing vertical mixing and acting as a barrier between the surface waters and the warm Atlantic water below. Sea ice has been shown to be an important component in many globally important climate processes, such as sea ice formation related deep water formation, driving cold deep-water currents out from the Arctic (Aagaard and Carmack, 1989; Serreze and Barry, 2005b).

2.1.1 Surface energy balance over sea ice

The net energy flux at the sea ice surface represents the sum of atmospheric and oceanic heat exchange. The surface energy budget accounts for radiative, turbulent and conductive heat fluxes as illustrated in figure 1. We follow the definition of the net energy flux used in Else et al. (2014); Persson et al. (2002):

$$F_{net} = R_{net} - H_S - H_L + C, \tag{1}$$

where the net energy flux at the surface, F_{net}, consists of R_{net},the net radiative flux, H_S, the sensible heat flux, H_L, the latent heat flux and C, conduction. Radiative fluxes and the conductive flux are defined positive when directed towards the surface and turbulent fluxes are positive when directed away from the surface.

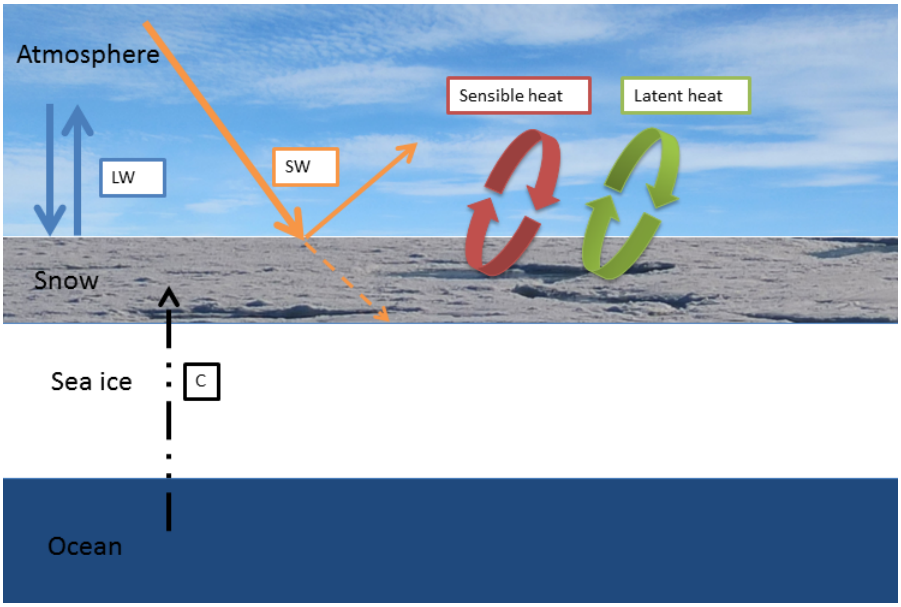

Figure 1: Illustration of surface energy balance components (SW = short-wave radiation, LW= long-wave radiation, C = conductive heat) Curved arrows represent turbulent exchange

The radiation term can be further split into terrestrial radiation (LW), wavelengths $4 - 300\mu m$, and solar radiation(SW), wavelengths 0.15 - 4.0 μm;

$$R_{net} = R_{LW} \downarrow + R_{LW} \uparrow + R_{SW} \downarrow + R_{SW} \uparrow, \tag{2}$$

where the arrows represent up-welling and down-welling. In addition, some portion of the down-welling short wave radiation is transmitted through the ice into the ocean beneath. Else et al. (2014) show that the transmitted irradiance is relatively small, especially when snow cover is present, and associated with a large uncertainty. Hence, transmitted irradiance is not accounted for in this work.

The reflectivity of the surface (albedo), α, dictates the short-wave radiation balance over a surface. The short-wave net radiation at the surface equals:

$$R_{SWnet} = R_{SW} \downarrow (1 - \alpha), \tag{3}$$

The albedo is simply the ratio between the incoming and outgoing short-wave radiation. The second column in Table 1 summarizes typical surface albedo values relevant for the sea ice environment.

Longwave radiation is a function of the surface skin temperature,

$$R_{LW} \uparrow = \varepsilon \sigma T_{skin}^4, \tag{4}$$

where ε is the emissivity of the surface and σ is the Stefan-Boltzmann constant 5.67 x 10^{-8} W $m^{-2}K^{-4}$.

Table 1: **Reflectivity (albedo) and conductivity properties of surfaces typical to sea ice melt season**

Surface type	Albedo (α)	Thermal conductivity (k) [W m^{-1} K^{-1}]
Fresh snow	0.7-0.9	0.06
Melting snow	0.5-0.6	0.42
Thick first year ice	0.3-0.6	2.24* (pure at 273.15 K)
Meltponds on sea ice	0.15-0.4	0.57* (fresh water at 281.15 K)

* Properties are temperature and salinity dependent *Source:* (Serreze and Barry, 2005a; Oke, 1987)

Snow and ice surfaces are relatively close to a black bodies in the long wave spectrum, with a typical emissivity of 0.98 to 0.99 (Serreze and Barry, 2005a).

Turbulent fluxes act to establish equilibria between the surface and the overlaying atmosphere. The magnitude and direction of these fluxes depend on the gradient of the scalar of interest and the turbulent kinetic energy available for mixing. Sensible and latent heat fluxes are commonly treated as purely turbulent, the conductive component being comparatively very small.

Turbulent fluxes were calculated using Eddy Covariance - methodology (EC) Aubinet et al. (2012), described in detail in section 2.3.1. The sensible heat flux, H_S ([W/m^2]) being :

$$H_S = \overline{\rho_d} c_p \overline{w'T'}, \tag{5}$$

where ρ_d is the dry air density,c_p is the heat capacity of air, 1004 J kg^{-1} K $^{-1}$ and $\overline{w'T'}$ is the covariance between the turbulent part of temperature (T) and the vertical wind component (w).
Similarly, the turbulent flux of latent heat, H_L ([W/m^2]), is

$$H_L = \overline{\rho_d} \lambda \overline{w'q'}, \tag{6}$$

here q is the specific humidity and λ is the latent heat of vaporization for water ([J kg^{-1}]),

$$\lambda = 3147.5 - 2.372\Theta, \tag{7}$$

where Θ is the potential temperature.

The last term in the surface energy budget is the conductive heat flux, C.

$$C = -k\frac{\Delta T}{\Delta z}, \tag{8}$$

where k is the thermal conductivity of snow or ice and $\frac{\Delta T}{\Delta z}$ is the vertical temperature gradient on snow or ice. Here wee used the same values as Else et al. (2014), k_{snow}

= 0.3 W m^{-2} K^{-1} and k_{ice} = 2.0 W m^{-2} K^{-1}, from Sturm et al. (2002); Persson et al. (2002). Note that these values are somewhat different from the conductivity values in Table 1.

2.1.1.1 Melt season

Length and timing of Arctic sea ice melt season is a strong control of the surface energy budget. Recent decades have shown a shift towards earlier melt onset in the Arctic (Markus et al., 2009; Maksimovich and Vihma, 2012). Of all Arctic seas East Greenland Sea shows the strongest negative trend of 7.3 days earlier melt per decade (Markus et al., 2009). Maksimovich and Vihma (2012) reports a local trend of 9 days earlier snow melt onset per decade for the central Arctic Ocean for the 20 year period from 1989 to 2009. Accordingly the melt season for the whole Arctic has lengthened with approximately 20 days in the last 30 years. Again the largest trends are seen in East Greenland Sea with a melt season lengthening over 10 days per decade (Markus et al., 2009). In the seas with the most extensive ice retreat the combination of early melt and late freeze-up has lengthened the ice free period with three months compared to the ice season 1979-1980 (Stammerjohn et al., 2012).

Earlier melt onsets have been connected above all to increased downward long-wave radiation. A re-analysis data based study by Maksimovich and Vihma (2012) shows that inter-annual variability in snow melt onset in the central Arctic was in 65 % of the cases explained by a surface energy budget anomaly 1-7 days prior snow melt onset and, downward longwave radiation was the most significant term in the anomalies. Similar results are reported by detailed case studies from different campaigns. Based on SHEBA data from the Beaufort Sea Persson (2012) shows that snow melt onset was primarily driven by an increased downward longwave radiative flux accompanied by a modest albedo decrease. Also Else et al. (2014) concludes that the melt onset was triggered by a low long-wave radiative loss due to cloud cover and the gradual seasonal increase in solar radiation with a decreasing albedo.

A longer open-water season yields in more heat and moisture input from the ocean. Early sea ice melt leads to a greater accumulation of heat in the surface waters. The warmer waters require more time to cool down and delaying the autumn freeze-up takes place later. Heat fluxes from the ocean have increased in the autumn and early winter with the sea ice retreat (Stroeve et al., 2012).

Both Persson (2012) and Else et al. (2014) connect melt onset with synoptic events advecting warm and moist air into the Arctic. Atmospheric eddies are an important mean of the poleward heat transport (Serreze and Barry, 2005b) and the role of individual cyclones and storms is expected to strengthen with thinner, mechanically weaker ice. Open water fractions and wind induced surface mixing

will further affect the ice and the surface energy budget.

After the melt onset the surface energy balance is driven by the surface albedo evolution. In general, snow is a good reflector having a high albedo, decreasing with snow age and wetness (Warren, 1982). Albedo values in Table 1 show that melts season evolution is accompanied with a significant albedo drop, enhancing short-wave absorption. This is the fundamental mechanism of the positive albedo feedback. As an example Else et al. (2014) reports an albedo drop from 0.85 to 0.25 during the melt season in the Canadian Arctic.

Compared to multi-year ice, seasonal sea ice has a thinner snow cover and also the ice itself is thinner. Thinner ice has less air bubbles scattering light yielding in a lower albedo. Also melt ponds are more extensive on thin ice as less ice deformation takes place and the ice has a smaller free board (Perovich and Polashenski, 2012). The albedo decrease generated by melt ponds is a strong driver of ice melt. A modelling study by Flocco et al. (2012) shows a 40 % higher September sea ice volume minimum in a melt pond free scenario.

Compared to radiation, turbulent fluxes over Arctic sea ice are in general small (Serreze and Barry, 2005a). Large fluxes are typically related to thin ice or open-water fractions, such as leads and polynyas. Else et al. (2014) observed small turbulent fluxes, with a diurnal cycle over sea ice prior melt onset. H_S was between -5 and 7 W/m^2 , with a net contribution close to zero, and latent heat flux cooled the surface the whole spring, through sublimation prior to melt onset and as evaporation afterwards. H_L cooled the surface at rates between -2 and -9 W/m^2.

The diurnal signal in both H_S and H_L disappears after snow melt and fluxes are hereafter controlled by synoptic activity (Else et al., 2014; Persson et al., 2002). For sensible heat flux this is explained with the snow pack getting isothermal at melting point, phase changes determining energy exchange. The constant surface temperature explains also the sustained large heat input to the surface in connection with a cyclone passage after melt onset with a H_S 3h average maximum around 40 W/m^2. The net effect of the synoptic event was balanced by excessive evaporation cooling the surface with a H_S hourly maximum at 40 W/m^2.

Snow on top of ice is also an important insulation between the air and the ice (see Table 1 for snow and ice heat conductivities. Prior melt Else et al. (2014) reports a diurnal cycle also in the conductive heat fluxes, with fluxes ranging between -6 and 7 W m^{-2} with the net contribution being close to zero. As sea ice gets isothermal during the melt season the conductive heat flux diminishes close to zero. With a shortened sea ice season less of the precipitated snow accumulates the ice, further weakening the ice. Also summertime precipitation shift from snow to rain is suggested to have increased the fraction of bare ice (Screen and Simmonds,

2012).

Sea ice retreat has been connected to decreased static stability in the atmospheric boundary layer. The Arctic boundary layer over sea ice is predominantly stable or near neutral. A negative radiative balance at the surface and warm air advection higher up in the atmosphere drives formation of strong surface based temperature inversions. This phenomena is most pronounced in winter months, whereas, summertime inversion are typically deeper and elevated, capping a near-neutral layer(Vihma et al., 2014; Serreze and Barry, 2005a). Shallow stably stratified boundary layer has low heat capacity connecting the sea ice retreat and the amplified climate change in the Arctic (Esau and Zilitinkevich, 2010).

Convective situations in the sea ice environment are typically related to coexistence of ice and open-water, such as leads and polynyas. Open-water is a source of both temperature and moisture, shaping the down-wind side over ice conditions. Local convection is also a source of turbulent energy to the ABL. The influence of these features is strongest in wintertime, when the temperature differences are at largest. As the ice gets thinner and weaker the fraction of open water areas is expected to increase.

2.2 Carbon cycling in the Arctic sea ice environment

As mentioned in the introduction, world oceans are a major sink for atmospheric CO_2. According to the 5th IPCC report (Ciais et al., 2013) the ocean sink strength was 2.4 ± 0.7 PgC yr^{-1} averaged for 2004 to 2011. This makes a considerable part of the 9.5 ± 0.8 PgC anthropogenic emissions(in 2011). Estimates of the net CO_2 uptake by the Arctic Ocean ranges from 66 to 199 Tg C yr^{-1} (Arrigo et al., 2010; Bates and Mathis, 2009; Takahashi et al., 2012). However, the role of sea ice on the carbon cycling in the Arctic has received relatively little attention (Parmentier et al., 2013). A simplified illustration of carbon cycling in the Arctic is presented in Figure 2. Only fluxes affected by changes in sea ice conditions are shown.

Three main mechanisms are put forward as 'pumping' carbon dioxide into the Arctic Ocean are affected by sea ice. The 'brine pump', or 'sea ice pump', is driven by thermal, chemical and physical properties of sea ice itself, whereas the solubility pump and the biological pump, forming the shelf pump, reflect sea ice induced changes in surface waters. Sea ice surface properties such as snow cover and melt ponds affect carbon exchange together with other sea ice features. Especially, polynyas are recognized as hot spots for CO_2 fluxes in the Arctic (Else et al., 2011). Even indirect interactions between sea ice and terrestrial areas are shown to alter the carbon balance in the Arctic (Bhatt et al., 2010).

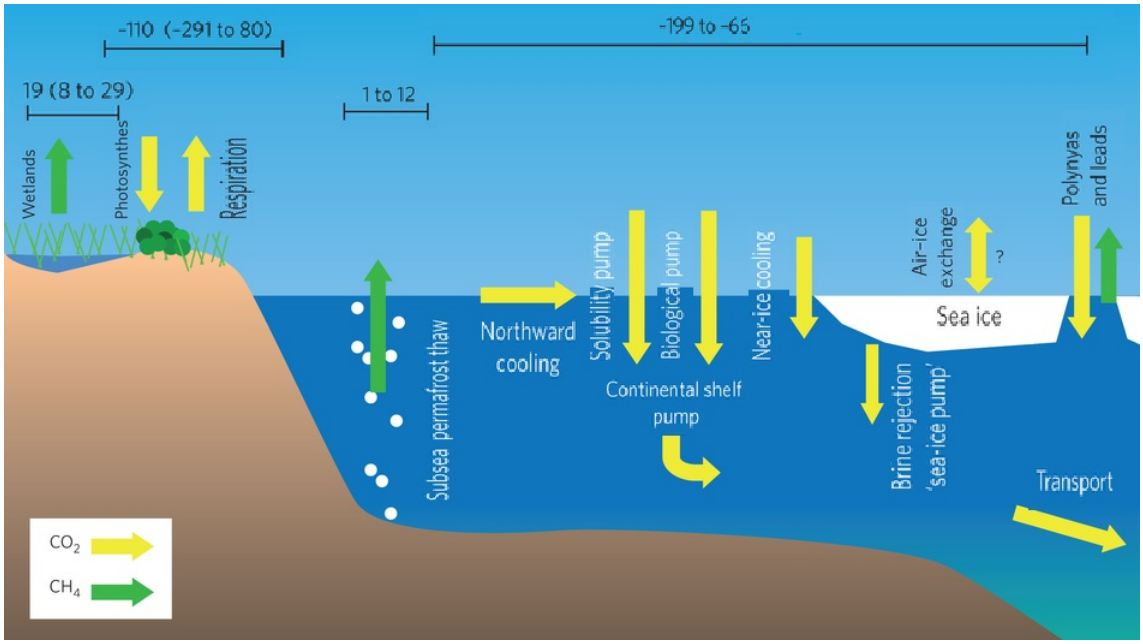

Figure 2: Representation of carbon fluxes possibly modified by sea ice retreat. Number ranges in the top panel indicate the source/sink strength (positive/negative) based on conducted studies in Tg C yr^{-1} *source:* Parmentier et al. (2013)

Carbon cycling in the Arctic do not solely consist of CO_2. Another important greenhouse gas is methane, CH_4. Opposite to carbon dioxide, Arctic is a net source of methane according to current estimates (Parmentier et al., 2013). Methane effluxes from tundra are estimated be in the order of 19 Tg C yr^{-1} with an uncertainty range between 8 Tg C yr^{-1} to 29 Tg C yr^{-1}. With thawing subsea permafrost, the oceanic part of the methane budget may be of similar size to the terrestrial. The knowledge level of air-ocean methane flux trends, however, remains low (Parmentier et al., 2013). It has been suggested that the occurrence of leads in sea ice may enhance oceanic CH_4 release, but the uncertainty is too high to assess the quantitative impact.

2.2.1 Solubility pump

Fundamentally CO_2 fluxes are driven by an air-ocean concentration gradient ($pCO_{2\ ocean} \neq pCO_{2\ atmosphere}$), making low pCO_2 surface waters sink regions. Oceanic surface pCO_2 typically controls the CO_2 exchange, as the atmospheric concentrations show relatively little variation. CO_2 solubility is a function of temperature and salinity, with fresh cold waters having the greatest dissolving capacity (Takahashi et al., 1993).

Due to the carbonate buffer system, the ocean is capable to uptake considerably more carbon than expected on the basis of solubility alone. In a given temperature

two chemical factors determine the CO_2 equilibria of surface waters: (a) the amount of dissolved inorganic carbon (DIC), referring to CO_2(aq), bicarbonate (HCO_3^-) and carbonate (CO_3^{-2}) and (b) the alkalinity of the water. Carbon dioxide dissolves in sea water, forming first carbonic acid, but being further reduced to bicarbonate and carbonate (Sigman et al., 2010).

$$CO_2(aq) + H_2O \leftrightarrow H_2CO_3 \leftrightarrow HCO3^- + H^+ \leftrightarrow CO_3^{2-} + 2H^+. \tag{9}$$

(aq = aqueous form)

An alkalinity increase in constant conditions drives the reaction to the right in equation (9), lowering the pCO_2 when more DIC is in carbonate form. The opposite is true, if DIC is increased the equilibrium shifts to the left; CO_2(aq) increases and, somewhat non-intuitively carbonate concentrations decrease, making the water more acidic (Sigman et al., 2010).

The solubility pump refers to enhanced CO_2 uptake in wintertime open-water areas when surface waters are cooled. The pump is driven by cold dense waters sinking, removing CO_2 from the surface. Together with the biological pump, the solubility pump is a part of the do called continental shelf pump. It is estimated to strengthen with declining sea ice coverage as it translates to more direct air-ocean exchange (Parmentier et al., 2013).

2.2.2 Biological pump

Photosynthetic activity further reduces DIC and CO_2(aq) in and the waters. As soon as enough light can penetrate into the ice, this reduction can have large impacts on the sea ice sink strength (Gleitz et al., 1995). As melting sea ice finally breaks up more light reaches the surface waters and pelagic primary production starts. Throughout the summer pelagic primary production withdraw CO_2(aq) from the surface waters. Sinking algal cells establish a net carbon export to deeper waters. In literature this is called the biological carbon pump.

2.2.3 Sea ice pump (brine pump)

The sea ice pump is the overall effect of the sea-ice cycle on air-ocean carbon fluxes, from freeze-up to decay. Figure 3 illustrates the concept of carbon exchange in ice covered seas. This pump accounts for brine rejection from ice as it forms, the air-sea exchange cut-off in winter, the effects of fresh, low alkalinity melt water and the biological activity in and under ice in summer months (Rysgaard et al., 2011). However, despite being a net pump, sea ice also generates efflux of CO_2 during ice freeze up.

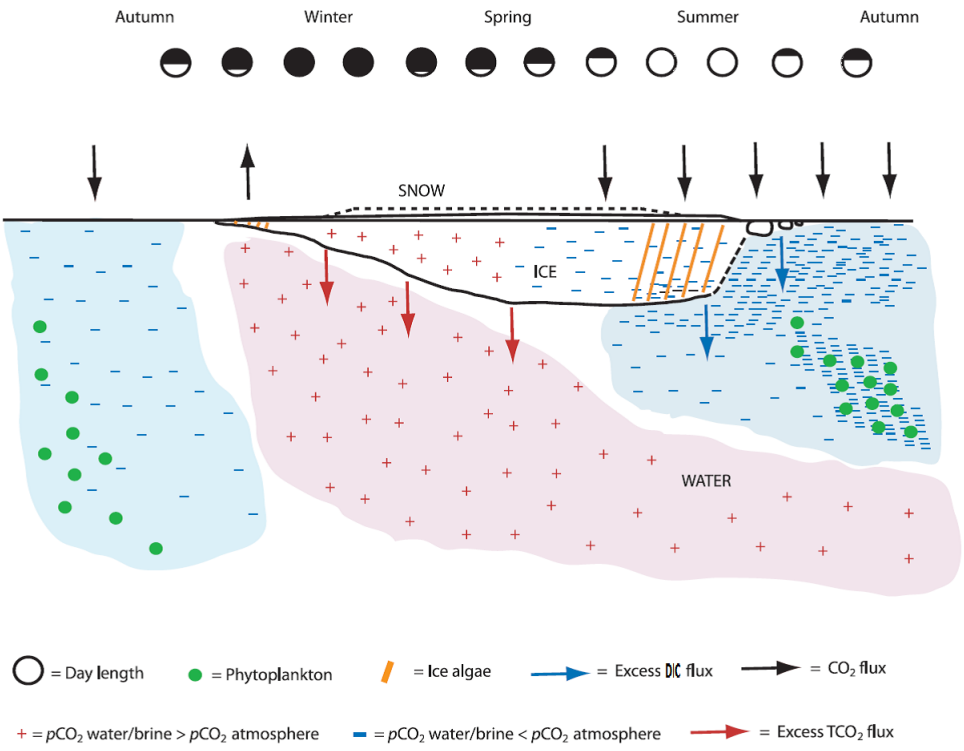

Figure 3: Simplified conceptualization of the seasonal cycle of CO_2 exchange in ice covered seas*source:* Rysgaard et al. (2011)

Sea ice permeability is the dominant control of gas exchange through sea ice. Unlike fresh water ice, sea ice is always a combination of salty liquid inclusions (brine), gas bubbles and ice. Brine volume is a function of salinity and temperature. Sea ice permeability is a measure of the connectivity of the brine network and the connectivity increases with increasing brine volume. Independent studies have shown that as brine volume exceeds 5 % a drastic increase in sea ice permeability takes place. This is roughly equivalent to ice temperatures around -7 °C(Golden et al., 2007; Pringle et al., 2009).

The first stage of sea ice formation is a porous ice crystal. The ice lattice rejects salts, trapping hyper saline ($S_{brine} > 35$ ppm) liquid in in brine pockets within the ice. This leads to high DIC concentrations in brine and, as explained above (equation 9), increased CO_2 concentrations. Surface cooling decreases brine volumes and pushes some of the CO_2 super saturated brines to the surface. This is the mechanism behind the freeze-up related CO_2 efflux. However, most of the brine ends up in the surface waters after brine drainage processes (Notz et al., 2003; Nomura et al., 2006).

After the freeze-up, long-wave radiative cooling of the surface creates a negative

vertical temperature gradient in the ice ($T_{surface} > T_{bottom}$). The brine volumes in the upper parts of the sea ice decreases and reduces, or completely hinders, gas exchange across the ice (Loose et al., 2011). Contracted brine volumes promote salinity, CO_2(aq) and mineral supersaturation . This has been shown to promote precipitation of calcium carbonate polymorphs ($CaCO_3$), especially ikaite($CaCO_3 \cdot H_2O$)(Dieckmann et al., 2008, 2010; Rysgaard et al., 2012; Rysgaard et al., 2013). The formation of calcium carbonates ($CaCO_3$), such as ikaite , in sea ice acts to reduce the alkalinity and increases CO_2 (aq).

$$Ca^{2+} + 2HCO_3^- \rightarrow CaCO_3 + H_2O + CO_2(aq) \tag{10}$$

If the brine network is connected ($V_{brine} > 5$ %), gravity drainage will act to neutralize the ice temperature gradient induced density gradient. This brine convection exchanges heavy, saline, brine with sea water (Notz and Worster, 2009). It is proposed that the $CaCO_3$ salts may be trapped in the ice skeletal, acting as an alkalinity reservoir (Rysgaard et al., 2007). Brine drainage introduces an density gradient in the water column driving a transport of CO_2 (aq) rich waters to deeper waters. Several wintertime studies conducted in the Arctic report both DIC and CO_2 supersaturated under-ice waters, supporting this theoretical framework (Rysgaard et al., 2007; Semiletov et al., 2004; Kelley, 1987). The suggested importance of brine rejection and deep-water formation on oceanic CO_2 uptake makes leads and polynyas potentially important for the sea ice pump driving continuous ice formation (Else et al., 2013). Additional, possible wintertime air-sea gas exchange presented in (Rysgaard et al., 2007) are: i) Sea-ice flooding events, as well as, ii) gas diffusion through the ice matrix and cracks in the ice.

Rising temperatures in spring and summer lead eventually to sea ice melt. As the melt starts brine pocket expand, increasing sea ice permeability allowing air-brine gas exchange. This makes the CO_2 enriched brine in the upper parts of the ice a potential CO_2 source for the atmosphere. However, melt water quickly dilutes the brine decreasing the CO_2 concentration and dissolution of trapped $CaCO_3$ will increase brine alkalinity and promote further CO_2 uptake. Both of these mechanisms acts to reverse the air-ice CO_2 gradient and, eventually, turn sea ice into a carbon sink.

Sea ice melt stratifies surface waters, as the fresh CO_2(aq) and DIC depleted melt water mixes with the under ice water. The calcium salts trapped in ice lower the melt water TA, thus further enhancing the air-sea CO_2 exchange. Independent studies from Baffin Bay, Canadian Arctic (Jones et al., 1983), the Arctic Ocean (Rysgaard et al., 2009) and coastal waters of East Greenland (Sejr et al., 2011) have reported evidence of sea-ice driven TA in surface waters.

Rysgaard et al. (2011) estimates the total sink strength of the sea ice pump in the Arctic to be 31 Tg C yr^{-1} , excluding $CaCO_3$ formation in sea ice reduces the sink to 14 Tg C yr^{-1}. These results were derived based on the conceptual

model presented above by using estimates of Arctic sea ice volume based on average thickness and coverage (Comiso and Nishio, 2008; Kwok et al., 2009) together with representative ice salinity, alkalinity and DIC values for Arctic (Rysgaard et al., 2009). Including calcium carbonate this accounts for 20% and even without for 9% of the open-water CO_2 uptake in Arctic waters (90°N to 62 °N) (Takahashi et al., 2012).

However, according to Rysgaard et al. (2011), it is hard to tell apart the roles of the sea-ice driven and the biological carbon pumps on big scales. Anyhow, a study conducted in north eastern Greenland Sea estimates these carbon pumps to be of roughly equal size.

2.2.4 Sea ice - land connection

As discussed earlier in this chapter, sea ice seems to be a strong controlling factor of near-surface temperatures in the Arctic (Deser et al., 2010; Screen et al., 2013). Higher temperatures increase plant productivity and respiration. The largest sea ice retreat related warming was discovered in the autumn, when incoming sunlight is limited. Autumn warming favors increased plant respiration over productivity, as its not light-dependent.

Increased surface temperatures lead to shorter snow covered periods. Earlier snow melt have been connected to increased terrestrial CO_2 uptake. However, several studies indicate that the increase in plant productivity uptake seems to level off, whereas respiration rates continue to grow with increased warming (Parmentier et al., 2011; Lund et al., 2012). Despite the high uncertainties, there are evidence that the terrestrial CO_2 sink is diminishing with retreating sea ice (Parmentier et al., 2013).

2.3 Methodology

2.3.1 Eddy Covariance theory

Eddy Covariance is a widely used method in micrometeorological flux calculations. The methodology builds on the idea that over flat and horizontally homogeneous surfaces the turbulent exchange equals the covariance between the turbulent part of the vertical wind component and the scalar of interest. The turbulent part is the fluctuating part of a Reynolds decomposed time-series (Aubinet et al., 2012).

$$s = \overline{s} + s', \tag{11}$$

Where overbar denotes the mean part, $\overline{s}$, and prime the deviation s'.

Thus, the turbulent flux, F_{EC}, is defined as:

$$F_{EC} = \rho_{dry}\overline{w's'}, \tag{12}$$

where ρ_{dry} is the density of dry air, w' and s' is the fluctuating part of the vertical wind component, w, and the scalar s respectively.

The theoretical basis of the Eddy Covariance method was laid already around 1950 by Montgomery (1948); Swinbank (1951); Obukhov (1951). The lack of sophisticated enough high-frequency instrumentation limited the application of EC in the early days. First modern, three dimensional, anemometers where developed in the 60's. Finally, the first continuous EC measurements didn't start before 1990, when new generation sonic anemometers and infrared gas analyzers together with sufficient software packages were available (Aubinet et al. (2012)).

2.3.2 Atmospheric surface layer

The EC methodology builds on the assumption that the measurements are carried out in the atmospheric surface layer. This layer is sometimes also referred to as the *Prandtl layer* or the *constant flux layer* and is directly affected by the drag of the surface. Typically the surface boundary layer makes up for the lowest 10% of the atmospheric boundary layer. The surface layer air-surface exchange is dominated by turbulence, justifying the use of EC technique, and the turbulent fluxes are approximately constant with height. Figure 4 illustrates the theoretical flow structure, with a mean flow and turbulent variation, in the atmospheric boundary layer over fjord ice.

For neutrally stratified conditions ($\frac{d\Theta}{dz} = constant$, where Θ = potential temperature) over horizontally homogeneous terrain dimension analysis results in the following vertical flow profile (Stull (1988)),

$$\frac{z}{u_*}\frac{du}{dz} = constant = \frac{1}{k}, \tag{13}$$

where u is the wind component in the mean wind direction, u_* is the friction velocity (see equation) ,k is the *von Karman* constant, z height over ground and z_0 is the roughness length (height where u=0). This yield in the logarithmic wind law with a constant mean wind direction (Stull, 1988),

$$u(z) = \frac{u_*}{k}ln(\frac{z}{z_0}), \tag{14}$$

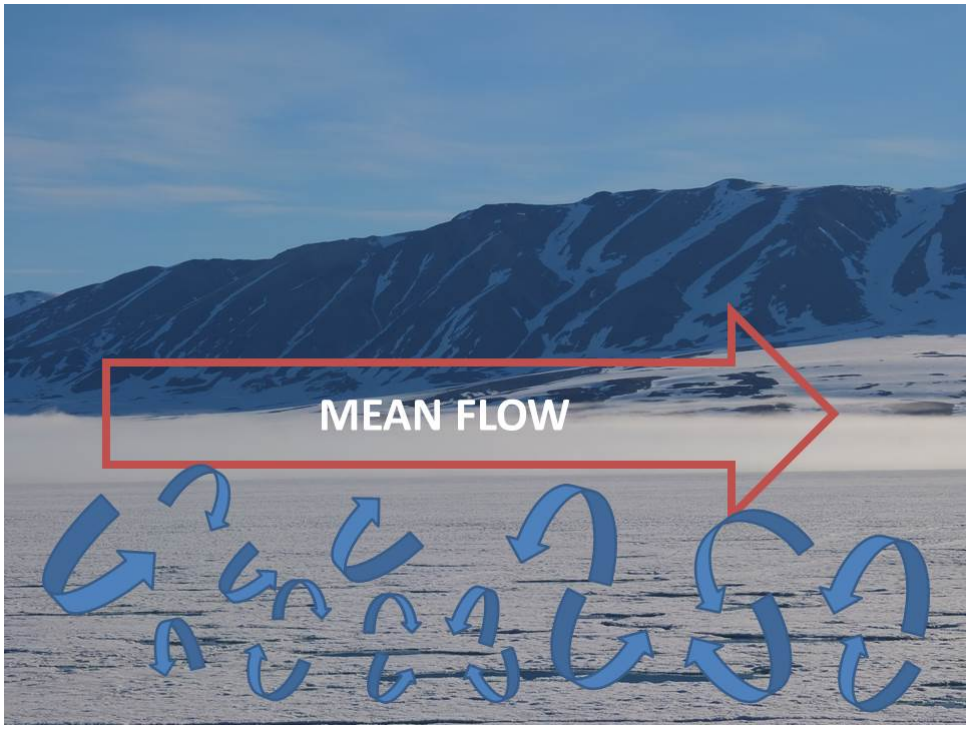

Figure 4: Schematic of surface boundary layer flow structures

Where u_* is the friction velocity, a velocity scale characterizing the shear at the boundary defined as,

$$u_* = \sqrt{\frac{\rho}{\tau}} = \sqrt{\overline{u'w'}}, \tag{15}$$

where ρ is the density of air and τ is the *Reynolds stress term* (turbulence induced vertical momentum flux (American Meteorological Society, 2014)).

Similarly a characterizing scale can be derived for temperature(Stull (1988)),

$$\Theta_* = \frac{\overline{\Theta' w'}}{u_*}, \tag{16}$$

2.3.3 Non-neutral conditions

Completely neutral conditions seldom prevail in the atmospheric surface boundary layer. In polar regions the boundary layer is stably stratified large parts of the year (Serreze and Barry, 2005c). The Monin-Obukhov similarity theory (hereafter M-O theory) is an extension to the neutrally stratified flow profile and it accounts also for the buoyant forces generating/suppressing turbulence. The stratification is described by the *Obukhov length*, describing the relationship between dynamic,thermal and buoyant processes (Stull, 1988):

$$L = \frac{-u_*^3 T_v}{kg\overline{w'T'_{v0}}}, \tag{17}$$

where T_v the virtual temperature, g is the gravitational force, $\overline{w'T'_{v0}}$ is the surface virtual temperature flux (rest of the variables are explained with equation 14).When buoyancy is creating turbulence (unstable conditions) and, vice versa, when buoyancy suppresses turbulence $L < 0$.

For a dimensionless stability parameter the measurement height is divided by L,

$$\zeta = \frac{z}{L}. \tag{18}$$

The advantage of using ζ is that, unlike L, it doesn't go to infinity in neutral situations ($\overline{w'T'_{v0}} \rightarrow 0$). Table 2 summarizes the interpretation of the stability measures L and ζ.

Parameter[unit]	stable	neutral	unstable
L [m]	<0	∞	>0
ζ [ ]	<0	0	>0

Table 2: Stability parameters

Equation 13 can be expressed for non-neutral situations by utilizing the stability parameter, ζ.

$$\frac{z}{u_*}\frac{du}{dz} = \frac{1}{k}\phi_m(\zeta), \tag{19}$$

where $\phi_m(\zeta)$ is a stability dependent dimensionless function. $\phi_m(\zeta)$ is needs to be empirically determined, and if the theorem holds it should be independent of time and space, 'universal'. Similarly there is an universal function, $\phi_h(\zeta)$, for vertical profile of temperature (u is replaced by Θ) (Stull, 1988).

2.3.4 Bulk algorithm for turbulent fluxes

Equations 6 and 5 in section show calculation of EC derived latent and sensible heat. For comparison a bulk algorithm was used for flux calculations. The bulk aerodynamic formula assumes a well-mixed boundary layer, so that the turbulent momentum flux depends on a surface drag coefficient and the wind speed (Holton, 2004). Hereafter surface fluxes can be represented with vertical gradients of the studied scalar (Andreas, 2002; Andreas et al., 2010; Savijärvi and Vihma, 2001).

$$H_S = \rho c_p C_{HS} u(z)(\Theta_0 - \Theta_z) \tag{20}$$

$$H_L = \rho \lambda C_{HL} u(z)(q_0 - q_z) \tag{21}$$

The empirical drag coefficients, C_{HS}, C_{HL} are derived from the M-O similarity theory and include empirical functions of the Obukhov length, L (see section 2.3).

$$C_{HS} = \frac{k^2}{[ln(\frac{z}{z_0}) - \psi_m(\zeta)][ln(\frac{z}{T_*}) - \psi_h(\zeta)]} \tag{22}$$

$$C_{HL} = \frac{k^2}{[ln(\frac{z}{z_0} - \psi_m(\zeta)][ln(\frac{z}{q_*} - \psi_h(\zeta)]} \tag{23}$$

3 Materials and Methods

Figure 5: Location of Daneborg in Greenland

3.1 Campaign and study area

The Young Sound 2014 campaign was organized and funded by the *Arctic Science Partnership* consortium. This work contributes to the project *Greenhouse gas exchange and the carbon cycle in the Arctic coastal areas*. The campaign was divided into three different working legs between 29th April and 2nd July 2014.

Young Sound is a high Arctic fjord located in North East Greenland. The fjord is connected to Tyrolerfjorden and together they make up a 90 km long and 2-7 km deep sill fjord system with a mean depth of 100 m (Rysgaard and Glud, 2007). Young Sound opens into the southward flowing East Greenland Current (EGC) transporting cold water masses and ice out from the Arctic (Buch et al. (2007) in (Rysgaard and Glud, 2007)). Young Sound fjord bears a roughly 160 cm thick ice-cover large parts of the year. The on-ice snow cover varied between 20 and 100 cm. In a 50 year time series up to 2007 the number of ice free days ranged from 63 to 131 days. The last 10-15 years of the time series reveals a trend toward more ice free conditions in the fjord. Seven of the longest ice free periods were recorded after 1990 (Rysgaard and Glud, 2007).

Typically for a high Arctic fjord Young Sound is surrounded by complex topography. Mountains, valleys and glaciers create orographic effects such as wind channelling, drainage flows and gravity waves (Vihma et al., 2014). The surrounding orography steers the large scale synoptic flows to blow along the fjord.

The visible spectrum satellite image taken over Young Sound (Figure 6 a)reveals a polynya close to the fjord mouth, south-west of Sandøen island. Figure 6 shows also that the open water zone is 35 km outside the fjord mouth and the ice conditions change just south of Sandøen. In the image darker color of ice indicates thinner ice with less snow cover. Close by to the Zackenberg research station, the Zackenberg river discharges into the fjord being a considerable fresh water source (Rysgaard and Glud, 2007).

In addition to the Daneborg scientific station, the Danish military station Daneborg and Zackenberg ecological research station are located in the Young Sound fjord system, being sources of anthropogenic CO_2 emissions. The military station Daneborg is located right next to the Daneborg research station and Zackenberg ecological station is found further in the fjord, approximately 25 km from the flux station (see map in Figure 6 b).

The exact position of the micrometeorological towers was approximately on the mid-line of the fjord, roughly 2 km outside the research station in Daneborg (17° 18.546′ N 020° 13.739′ W). This was a compromise of distance from base and minimizing both flow distortion by surrounding topography and anthropogenic influence. The distance from the flux station to the fjord mouth was roughly 10 km (figure 6).

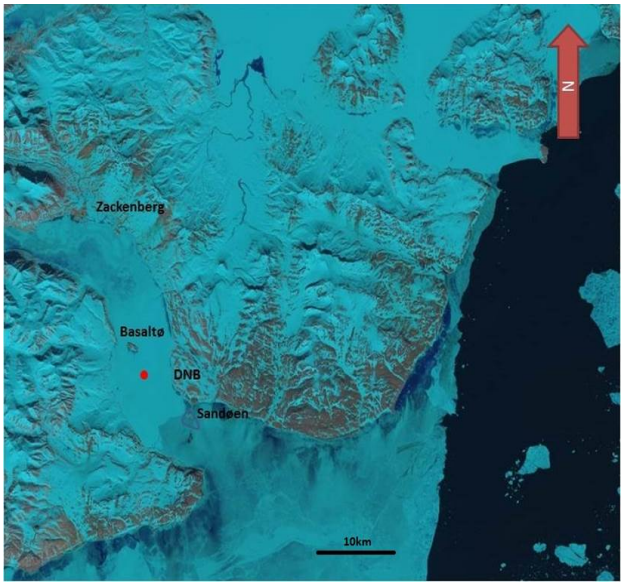

(a) Landsat 8 satellite picture 16th June 2014.Black areas are open water and blue snow or ice, where lighter colors indicating thicker ice.*Credit: National Snow and Ice Data Center/USGS/NASA/Landsat 8.*

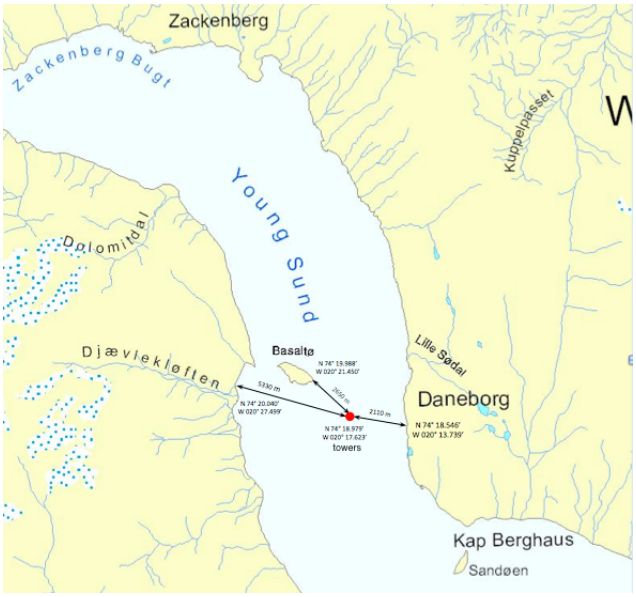

(b) Map of Young Sound (distances marked with black arrows for scale)

Figure 6: Tower position on Young Sound ice (red dot) with distances indicated with black arrows

3.2 Instrumentation and data collection

The author was present at the research station in Daneborg from June 13th until the end of the campaign. Fieldwork routines included instrumentation maintenance, instrument calibration and moving, re-building and taking down the masts.

Two masts were measuring turbulent CO_2 exchange over fjord ice in Young Sound. Both masts were equipped with sonic anemometers (CSAT3 and USA-1) and infra-red gas analyzers (Li7500). In addition, the other mast was equipped with basic weather station instrumentation. The first mast was built and secured directly into the ice (hereafter referred to as *Mast 1*, see figures 8) and, the other

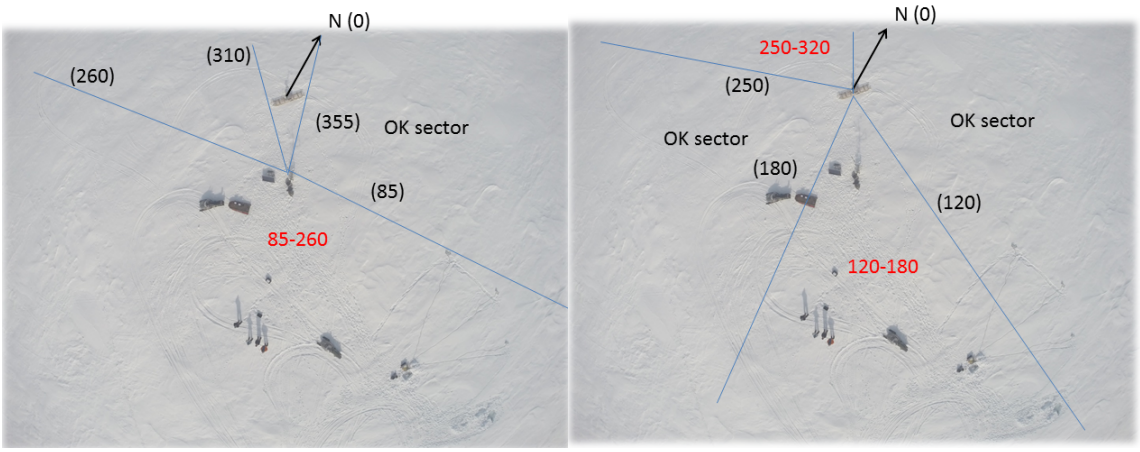

(a) (b)

Figure 7: a) Aerial picture of Mast 1 before June 19th and b) Mast 2. Lines are drawn to indicate contaminated wind directions (bad directions marked with red). North is 0°).

one was mounted on a sledge (hereafter *Mast 2*(Figure 9)).

Data of the surface water pCO_2 was collected at 2.5 m depth with a *CONTROS System & Solutions GmbH* underwater instrument roughly 1 km south of the masts. Every third (3.) day ice cores were taken close to the cite for ice together with on-ice snow temperature profiles. Basic weather station instrumentation was mounted on the other mast.

The masts were built in close vicinity of each other. Turbulence sensors placement was designed to minimize flow distortion by the towers. Figure 7 shows the tower placement and illustrates the contaminated wind directions. Note that this work follows the typical meteorological convention where a northerly wind direction equals 0 degrees. The sonic on Mast 1, in picture 7 a, was facing north, making southerly winds (85 to 260 degrees) contaminated by the mast itself. Mast 2, north-west of Mast1, blocked winds between 310 to 355 degrees.

As a consequence of surface melting Mast 1 sank into the ice and was moved and placed over pallets on June 19th (see Figure 8 b) As the flow was mostly from South-South-East (in-fjord) or North-Northwest(out-fjord) we decided to turn the sonic to face slightly north of east (85 degree) when Mast 1 was moved on June 19th. Hereafter the contaminated wind angles were 190 to 350 degrees. This turning of the anemometer allowed capture of both in- and out-fjord flow. The sonic on mast 2 (USA1 on figure 10 and in figure 7b), has theoretically a 360 degree view. However the gas analyzer contaminates winds around west and north-west (250 to 320 degrees) and in the opposite direction Mast 1 affects south-easterly winds (120-180 degrees).

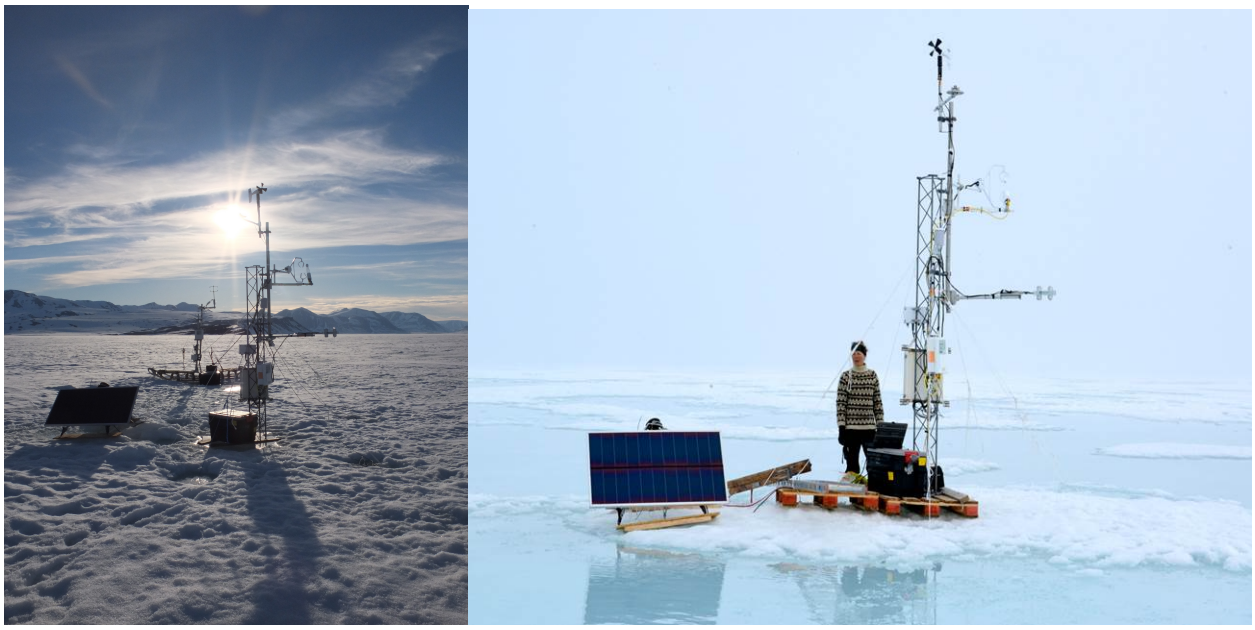

(a) (b)

Figure 8: Mast 1 with both meteorological instrumentation and high frequency turbulence sensors. a) before moving (Mast 2 is shown behind) and b) after being moved

The usage of two masts very close to each other is debatable, as this adds flow distortion. However advantage of this set-up is that the turbulent fluxes can be validated against each other. Especially with low fluxes it adds certainty to make double measurements. The original set-up shows a weakness in capturing south-easterly, in-fjord, winds. Unfortunately this also lead to a big part of the data from the first part of the campaign being discarded based on flow distortion.

The instrumentation on the flux masts was powered with two 12 V car batteries, connected in parallel, per mast. The batteries for Mast 1 were charged by two solar panels whereas the batteries of mast 2 were charged daily. Other daily maintenance included checking that the sensors and the masts were levelled and ice/frost free. All changes were carefully noted down and taken into account in the post processing of the raw data. When visiting the tower the sensor output was checked to detect possible sensor malfunction and USB stick/flash cards, storing the data, were changed regularly to secure the data. A weather log book was kept throughout the campaign. Gas analyzers were calibrated with known concentration N_2 and CO_2 gas (for details see section 3.2.1.3).

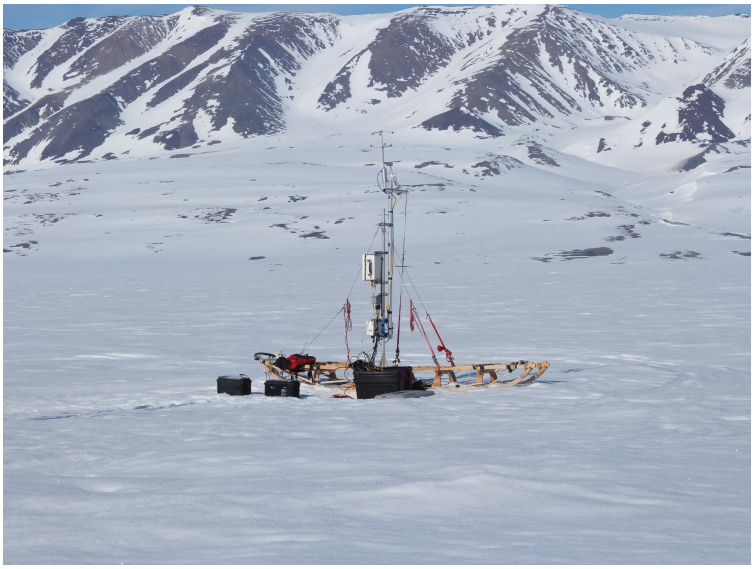

Figure 9: Mast 2, built on a sledge with high frequency sensors

	Mast 1	Mast 2 (sledge)
SA manufacturer	Campbell Scientific	Metek
SA sensor	CSAT3	USA-1
SA height [m]	2.6 - 3.2	3.1 - 3.21
IRGA	LiCor 7500	LiCor 7500
IRGA height	2,5-2,9 m	2,7-2,81
Data logger	Campbell CR3000	Li-7550 Analyzer interface

Table 3: Sonic anemometers (SA), infrared gas analyzers (IRGA) and dataloggers used in this study.

3.2.1 High-frequency Instrumentation

Table 3 summarizes the details of the high-frequency instruments and their installation heights. Wind, temperature, H_2O vapour, CO_2 and atmospheric pressure was collected with 10 Hz. As the study was conducted during the melt season the instrument height measured from the surface changed during the campaign, this is indicated with the height range reported in Tables 3 and 4. All the heights reported in table 3 are measured to the middle of the instruments.

3.2.1.1 Sonic anemometer (SA)

Two different sonic anemometers were used at the measurement cite (see Figure 3). Both anemometers, CSAT3 and USA-1, are commonly used for flux measurements, and the operation principles are the same. Sonic data is measurements of back and forth travel time of ultrasonic waves between three non-orthogonal transducer heads

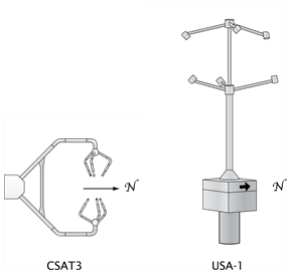

(a) (b)

Figure 10: Sonic anemometer on a) Mast 1 and b) Mast 2 and respective coordinate system indicated with north arrow *Source:* 2012 LI-COR, Inc.

(Instrument manual *Metek USA1*,Instrument manual *Campbell Sci. CSAT3*). The output is three wind components in x, y and z directions defined by the instrument coordinate system (see Figures 10 and 11). In addition to wind, a sonic temperature, T_s, is derived from the speed of sound between all three transducer pairs. Sonic temperature doesn't account for air humidity, so it resembles closely to virtual temperature, T_v.

The main difference in the anemometers are there coordinate systems and the structures of support(see figure 10). As figure 10 shows, the CSAT3 has a C-shaped design with the transducers at the tips. With this configuration only winds coming from behind the mast are sheltered. So only winds from within 30 degrees of the back of the sensor needs to be discarded In contrast, the USA-1 sensor has a pin supporting the transducer heads from the middle, possibly affecting one transducer pair for all wind direction. However the design is optimized so that the pin is thin and the contaminated transducer pair is close to perpendicular to the wind, having an almost zero contribution to the measurement. Previous studied by Mauder et al. (2007) comparing different sonic anemometers, show that the relatively big transducer heads of the USA1 may obstruct the flow.

The anemometers have different inbuilt coordinate systems, as illustrated in Figure 11. CSAT3 has a right hand coordinate system, with positive x-direction is into the boom, meaning opposite to instrument north (Figure 10) and USA-1 is left handed with positive u direction and instrument north being the same direction. This has consequences for the data processing presented in Chapter 5. Finally, a cross-wind correction is incorporated in CSAT3, but not in USA-1.

3.2.1.2 Infrared gas analyzers (IRGA)

Both masts were equipped with a LI7500 open-path IRGA, manufactured by LiCor (see figure 12). In the open-path design the sampling volume is not enclosed. The

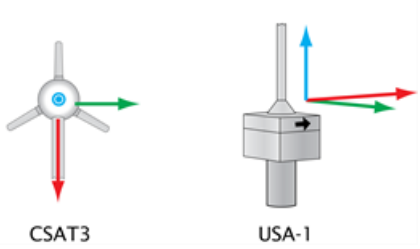

Figure 11: CSAT3 viewed from above and a perspective view on USA1 to demonstrate the difference in the sonic coordinate systems. Red arrows mark positive u direction, green arrows mark positive v direction, and blue arrow marks positive w. These are the orientations of the raw data provided by the instruments *Source:* 2012 LI-COR, Inc.

operation principle is based on CO_2 and H_2O absorption bands in the infra-red spectra. A decrease in radiant power between the transmitter and the detector, of a given wavelength in the absorption spectra of the gas of interest, is a non-linear function of the number density of the gas. The open-path analyzer operates by alternately transmitting radiation in an absorbing and in a non-absorbing reference band. In addition to the gas concentration the Li7500 comes with a high-frequency a pressure and temperature sensor (Instrument manual *LiCor inc. LI7500 sensor*).

An instrument specific correction for cross sensitivity and band-broadening is incorporated in the sensor calibration. Temperature and pressure changes the width of individual spectral lines of absorption and moisture in air alters the effective pressure of the gas mixture. This causes an relatively small, but possibly significant, overestimation of CO_2 in moist air (band broadening). Cross-sensitivity occurs if the transmission band corresponds to an absorption band of another gas present in the sampling volume. This generates over-estimation of the absorbing gas being measured. To differentiate CO_2 and H_2O optical filters are used to isolate species specific absorption bands from the infra-red radiation spectra. Another phenomenon is electrical cross-sensitivity due to delayed time response in the detector. The instrument operates by alternating the optical filter for CO_2 and H_2O with high frequency, even a small time lag in detection will cause uncertainty The LiCor-7500 does not take into account internally the dilution effect by foreign gases. This effect does not necessarily affect the measured number concentration, but it will affect the mole fractions. Especially if the mole fractions of a given gas in different gas compositions are compared the error may be significant (Instrument manual *LiCor7500*, Aubinet et al. (2012)).

An incorporated function converts the detector signal into a gas number density ($mmol/m^3$) with the aid of a calibration function and constants. This is the instrument output. The conversion of the output into a mixing ratio (mol/mol) the air density in the sample cell has to be accounted for. To account for fluctuations in the ambient air density open-path data needs to be density corrected. The widely

used density correction for open-path measurements is the Web-Pearman-Leuning (WPL) correction (Webb et al., 1980). In this work we chose to follow the density correction suggested by Sahlée et al. (2008)(For more details see data processing section). Sahlée's correction builds on calculating high-frequency time series of dry air density. Shortly, the advantages of this approach are that it not only corrects the flux, but also the spectra of CO_2 and H_2O and the correction is simple and easy to understand. It is worth stressing that, when compared, the WPL and Sahlee corrected fluxes differ very little (See the Results-section).

The greatest advantage of the open path analyzer is the reduced power requirement, compared to a closed-path sensor. In remote Arctic conditions, out on the fjord ice, this is essential. In cold conditions the inlet tube would need heating, requiring even more power. The only possibility to make continuous closed path measurements on fjord ice would involve a generator, which again would contaminate the CO_2 data. The open-path design is free from inlet tubing, and thus this design doesn't suffer from high frequency attenuation. This is also the reason the time lag between the IRGA and the sonic anemometer is typically very small.

A definite down-side with the open-path design is its exposure to weather. Precipitation and frosting may block the sensor windows resulting in malfunction. The instrument outputs a diagnostic number, to mark low quality measurements. However, the exclusion of poor measurements introduces data gaps, and thus uncertainty to time series. Another source of uncertainty is the many post-processing corrections applied to open-path measurements. The WPL correction includes the heat flux, increasing uncertainty. A correction introduced by Burba et al. (2008) corrects for the air density changes due to sensor-self heating or radiative cooling. The usage of this correction has been under debate. In low flux environments, like sea ice, these corrections can have severe consequences on the fluxes as the correction terms may be several orders of magnitude larger than the flux itself. However, a six years time series, presented by Haslwanter et al. (2009), of both open− and close-path measurements finds little over all difference in flux uncertainties. However, as pointed out in Aubinet et al. (2012) the comparably large correction terms makes it hard to determine the uncertainty of the flux among different conditions.

The large size and placement of the open-path IRGA is a source of flow distortion. This will possibly reduce the view of the sonic, making certain wind directions contaminated. However the gas analyser cannot be placed too far away from the sonic as this will violate the criteria of spatial averaging. The separation between the instruments should ideally be less than the smallest turbulent eddies present. Hence the path-length of both the sonic and The IRGA together with instrument separation limits the acceptable measuring height, as the smallest eddies are found closest to the surface (Aubinet et al., 2012).

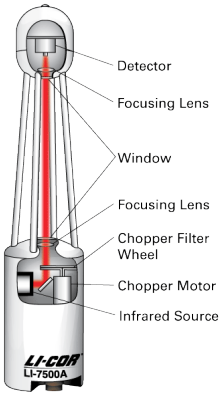

Figure 12: LiCor 7500 Open-path infrared gas analyzer used for flux measurements in Young Sound *Source:* 2012 LI-COR, Inc.

3.2.1.3 IRGA Calibration

Both IRGAs where calibrated by zeroing with nitrogen gas (N_2) and thereafter calibrated against a known concentration (400 ppm) CO_2 gas. A calibration tube was placed into the optical path and the tube volume was flushed with the zeroing gas and CO_2 at a constatnt rate. The manufacturer reports zeroed analyzers being stable for months, but large temperature variations affect the water vapor span stability (Instrument manual *LiCor7500*). Thus, the calibration frequency required depends on environmental conditions. In Young Sound the instruments were calibrated once each in June. The instrument offset is accounted for in post-processing of the data (Chapter 5).

3.2.2 Weather station instrumentation

Table 4 presents the 'slow-meteorology' instrumentation, with a measurement frequency once every 5 min, mounted on Mast 1. The instrumentation can be seen on the mast in Figure 8.

Parameter	Sensor (*Manufacturer*)	Height $[m]$
Temperature/ RH sensor	Campbell Scientific	~ 2
Surface temperature		~ 1.5
Wind(Speed & direction)	Young	
Long-wave radiation (↑↓)	CNR1 Net radiometer (*Kipp& Zonen*)	1.62
Short-wave radiation (↑↓)	CNR1 Net radiometer (*Kipp& Zonen*)	1.62

Table 4: Non-turbulent meteorology instrumentation mounted on Mast 1

Note that atmospheric pressure is not included in the weather station instrumentation, but was measured with the high frequency pressure sensor on Mast 2.

The radiation sensor was placed over snow but, as the melt season progressed, it was eventually measuring over extremely wet snow, at the edge of a melt pond.

3.2.3 Snow and ice data

Between May 26th and June 23rd ice cores and snow measurements were taken every third day at the tower cite. The cores were taken with a Kovacs drill corer with a 9 cm diameter. Snow measurements were made by digging snow pits. Snow and ice temperature was measured every 5 cm. In addition to the temperature data, snow depth, ice depth and ice freeboard was measured.

3.2.4 Under-ice pCO_2 measurements

The CONTROUS HydroC instrument measured under-ice oceanic pCO_2 with a 0.2 Hz frequency. The instrument was placed under ice roughly 1 km south of the flux tower and deployed at a depth of roughly 2.5 m. The measurement principle is based on non-dispersive infrared spectroscopy (NDIR). The dissolved oceanic gases reach equilibrium with the instrument headspace by reaching equilibrium through a hydrophobic membrane hereafter the concentration is measured within a gas circuit (Instrument manual *CONTROUS*). The data is saved by an internal data logger. A generator was kept running for energy supply. Thus, this cite is another source of anthropogenic CO_2 in the fjord environment.

3.3 Data-processing

High frequency data needs careful post-processing and quality control measures to be converted into reliable surface fluxes. Some of the post processing steps relate to the instrument design and some to the nature of turbulence. The application Eddy Covariance technique requires steady state conditions and a fully developed turbulence regime. Quality control is applied to ensure that the data fulfil this prerequisite. The micrometeorological community has quite well established data processing routines(Aubinet et al., 2012). No post-processing software was used in this work, but ready made codes were used as the base for the processing (original codes Lise Lotte Sørensen and Morten Nielsen) some examples were taken from *EddyUH*, developed at University of Helsinki (**?**). The author was responsible for all the data processing. All programs were written with MATLAB computing language.

In this work we chose to work with 28 min averaging periods, or differently put 17000 value blocks when measured with 10 Hz. The data processing is divided into raw post-processing, flux calculation and processing and quality control.

Variable	Max.value	Min. value
Wind (hor.)[m/s]	25	0
Wind (vert.)[m/s]	7	0
Temperature [°C]	25	-25
Pressure [hPa]	1080	600
CO_2 [mmol/m^3]	-	0
H_2O [mmol/m^3]	-	0

Table 5: Physical limits applied to the raw data

3.3.1 Raw data post-processing

3.3.1.1 IRGA calibration

The first step of post-processing is to correct the pre-calibration raw CO_2 and H_2O concentrations. The offsets for both towers are calculated by comparing CO_2 and H_2O concentrations before and after calibration. Thereafter the complete pre-calibration CO_2 and H_2O concentrations are corrected by the offset. The liability of applying one offset for the whole period can be questioned, as some instrument drift is expected. However, we estimate the drift to be negligible.

3.3.1.2 De-spiking raw data

Before calculating fluxes the raw data is cleaned from anomalous data points. Electrical noise, data transmissions problems, or disturbed measurements (frosting on IRGA as an example) can all cause spikes in the data. Several de-spiking methods have been proposed, in this work two are applied. First the data is scanned for non-physical values. The physical limits applied to this data are collected in Table 5. The discovered non-physical values were replaced with the previous approved value.

Also statistical testing for de-spiking, suggested by (Vickers and Mahrt, 1997), was performed on the data set. Mean value and standard deviation was calculated for a 5 min (9000 measurements) moving window over the raw time series.The window is moved forward 400 datapoints at a time. A spike is defined as,

$$|x_i - \overline{x_i}| \geq k \cdot \sigma_i, \tag{24}$$

where overbar marks the mean value and σ the standard deviation and i denotes the 5 min measurement window) k is the discrimination factor that is increased with 0.3 for each round of iteration, until the time series is spike-free. If three consequent measurements are defined as spikes it is interpreted as physical signal. Linear interpolation is used to fill in replace spikes.Following Aubinet et al. (2012)

1% of spikes was allowed in an averaging period.

As described in section 3.2.1.2 the gas analyser outputs a diagnostic value of the measurement quality. The raw data is scanned for diagnostic values and data with indication of malfunction (typically due to frosting on transducer or receiver windows) are removed.

3.3.1.3 Cross wind correction

As the sonic temperature is derived by using data from all three paths the wind effect needs to be accounted for. The CSAT3 sensor corrects for this internally. Sonic temperature measured with the USA-1 sensor is corrected for according to (Liu et al., 2001).

3.3.1.4 Coordinate rotation

For every 28-minutes averaging period the raw wind data is rotated into a Cartesian coordinate system with x-direction defined as the mean wind direction. As the time series is relatively short the 2^d rotation, instead of the planar-fit method, is applied to both sonics((**?**). The first rotation aligns the horizontal mean wind with the x direction(v= 0) and the second rotation zeroes the mean vertical wind ($\overline{w}$ = 0) (Kaimal and Finnigan, 1994). We are aware of the possibility of third rotation zeroing the lateral momentum flux $\overline{v'w'}$ (McMillen, 1988), but according to (Finnigan, 2004) this often yields in non-physical orientations of the flow-field and was therefore not applied to the data.

After rotating the wind data into Cartesian coordinates with respect to the sonic anemometer it is turned into geographic coordinates.

3.3.1.5 De-trending

The turbulent part of the time series, x', is resolved by removing the non-fluctuating part from the time series.

$$x' = x - \overline{x} \tag{25}$$

The non-fluctuating part, $\overline{x}$, is simply defined as the arithmetic mean of each 28 min averaging period (Block averaging method).

3.3.1.6 Sahlée - density correction

The raw gas concentration time series was corrected according to (Sahlée et al., 2008) as an alternative of the traditional WPL correction for the covariances (Webb et al., 1980). The advantages of this method is that the density correction is independent of humidity and heat fluxes, unlike the WPL correction and it gives

the possibility to examine co- ans power spectra of density corrected CO_2 and H_2O time series.

Sahlées correction builds on calculating high-frequency time series of dry air density. Shortly the advantages of this approach are that it not only corrects the flux, but also the spectra of CO_2 and H_2O and the correction is simple and easy to understand. It is worth stressing that, when compared, the WPL and Sahlée corrected fluxes differ very little. The Sahlée correction is mathematically fairly simple and it is based on the ideal gas law. This method requires high frequency temperature and air pressure measurements (available from the LI-7500 pressure and temperature sensor or the sonic temperature from the sonic temperature) for high-frequency dry air density data. Starting from raw CO_2 and H_2O measurements in $\frac{mmol}{m^3}$, χ_c andχ_c. For clarity all units are converted into SI units (K, kg, mol, J).

First the water vapour measurements are used to calculate the partial pressure of water vapour,e,for determining dry air density, $p_d = p - e$,

$$e = \chi v M_v T \frac{R_d}{\varepsilon} \tag{26}$$

Where M_d and M_v are the molar masses of dry air and water, ε is their ratio $\frac{M_v}{M_d}$ and R_d is the dry air gas constant (287.06 J kg^{-1} K^{-1})). Hereafter the dry air density and molar density are calculated.

$$\rho_d = \frac{p_d}{R_d T} \tag{27}$$

$$\chi_d = \frac{\rho_d}{M_d} \tag{28}$$

Then the density corrected molar mixing ratios are,

$$c_{mol} = \frac{\chi_c}{\chi_d}, \tag{29}$$

$$q_{mol} = \frac{\chi_v}{\chi_d}, \tag{30}$$

and further the mass mixing ratios,

$$c_{kg} = c_{mol} \frac{M_c}{M_d}, \tag{31}$$

$$q_{kg} = q_{mol} \frac{M_v}{M_d}, \tag{32}$$

CO_2 concentrations are reported in $\frac{\mu mol}{mol}$ and H_2O in $\frac{mmol}{mol}$. This correction also accounts for the change of units.

3.3.1.7 Sonic temperature correction

The sonic temperature is converted to actual air temperature following Kaimal and Gay (1991) in (Aubinet et al., 2012).

$$T = \frac{T_{sonic}}{1 + 0.32\frac{e}{p}} \tag{33}$$

3.3.2 Covariances

3.3.2.1 Spectral correction

No actual spectral corrections are applied to this data. However some averaging periods are filtered out based on inspection of power and co-spectra indicating a non fully developed turbulent regime (Sørensen et al., 2014).

The power and co-spectra of turbulent flow components and the measured trace gases are inspected in context of the general turbulence theorem (Kaimal and Finnigan, 1994). The spectra is normalized so that different moments can compared despite different stability and flow conditions.

4 Results

This chapter presents the turbulent CO_2 flux data, and complimentary atmospheric, sea ice and oceanic measurements, collected over first year fast fjord ice in Young Sound and all the data presented hereafter have gone through thorough post-processing and quality control routines (see Chapter 3 *Materials ans Methods*). This leads to abig data loss and the temporal coverage is reduced. Flux tower 2 data is available between May 30^{th} and June 26^{th} (28 days) and tower 1 data, including weather station data ,between June 4^{th} and June 27^{th} (23 days). The good quality data covers 240 hours.

Despite the reduced data, the time series captures the melt onset and eventually the formation and evolution of melt ponds. To present the results in context of the surface conditions the dataset is divided into three sub-periods - pre-melt, snow melt and melt pond. A similar approach is taken in Else et al. (2014). We base the division on visible changes to the snow. The pre-melt period is defined as the period with a seemingly uniform snow cover on the fjord (June 4^{th} and June 9^{th})(see figure 10). After the snow melt onset the surface got somewhat darker and started to appear 'bumpy'. The snow was very wet and slushy. Gradually melt ponds started to form. June 19^{th} the surface was clearly melt pond covered, and marks the start of the melt pond phase. The mean atmospheric, oceanic and surface energy exchange conditions divided into these sub-periods are listed in tables 6 and 7. For visualization of the surface conditions see Figure 10 for pre-melt and Figure 9 a and b for snow melt and melt ponds respectively.

4.1 General conditions

4.1.1 Atmospheric conditions

The atmospheric pressure was generally high during the campaign, ranging between 1010,4 hPa (June 7^{th}) and 1029,0 hPa (June 9^{th}) with a mean pressure of 1018,8 hPa. Figures 13 and 14 (see page 48) show temperature, humidity and wind evolution during the campaign. The temperature range is between -6.1 and 10.7 °C, with a clear diurnal pattern until the melt pond period. The minimum is observed June 4^{th} 3.40 am and the maximum June 10^{th} late in the afternoon. Humidity lies between 26.1 and 70.1 % (June 10^{th} and June 21^{st} respectively).

As expected, the prevailing wind directions where along the fjord axis (Figures 14 and 15). Most of the time the flow was in-fjords (from the ocean), but interestingly the highest wind speeds were observed with out-fjord flow. Northwesterly flow seems to be under represented in Figure 15, indicating shielding of the nearby island, Basaltøn (Map in Figure 7). Figure 15 is compiled from weather station

data,with no wind directions discarded due to flow distortion.

The wind reached its maximum, 12.3 m/s from North-Northeast, on June 8^{th} around the time of melt onset. Hereafter a shift in conditions occurred, temperatures increased, humidity dropped and the wind calmed down and the direction became variable (Figures 13, 14 and Table 6). Before the wind maximum, over a short time, the pressure increased and the wind picked up, indicating synoptic scale changes in the general weather.

The ongoing melt is encompassed in the different behaviour of temperatures at the surface and at 2 meters (Table 6).In the pre-melt season both the surface and the air above had a mean temperature of roughly -2.5 °C. The mean surface temperature is just below zero with a small deviation from the melt onset onwards being roughly half a degree warmer during the melt pond period than during snow melt. The mean air temperature is almost 5 degrees warmer in the snow melt period with a big standard deviation demonstrating a large diurnal cycle. In the melt pond phase the air temperature drops below zero and becomes colder than the surface with a standard deviation of 0.84 °C.

Table 6 summarizes the differences between the different phases of the melt season. The transition from snow melt to the melt pond period is marked with stabilizing atmospheric conditions. Especially temperature and humidity shows a clearly smaller range of variation in the melt pond period (Figure 13). Also the highest mean wind speeds and stable wind directions, with the flow being mainly in-fjords characterize this period.

The mean atmospheric CO_2 concentration drops from 400.37 ppm before melt onset to 396.06 ppm with melt ponds present (Table 6). The standard deviation is constant, around 3 ppm for all sub periods.

4.1.2 Sea ice and surface water conditions

Between May 26^{th} and June 23^{rd} 47 cm of snow on top of the ice melted at the measurement cite, leaving 14 cm snow on the ice between melt ponds. The sea ice itself melted only 7 cm from 140 cm to 133 cm. Figure 16 shows nicely how the core temperature increases with time and that the minimum temperature shifts lower down in the ice. All cores also reveal a C-shaped temperature profile, becoming more pronounced with time. Corresponding ice core salinity would show melt-induced desalination. The freezing point of sea water in Young Sound is roughly - 1.8 ° C. From June 17 th onwards the ice bottom was above -1 ° C, clearly indicating melt. However, under-ice fresh water from surface melt may slow down the bottom melt. The ice temperature at the snow interface shows the same warming over time. The ice temperatures were above the permeability threshold in

	Pre-melt	**Snow melt**	**Melt ponds**
Temperature(2m) [°C]	-2.5 ± 2.1	2.3 ± 2.1	-0.7 ± 0.8
Surface temperature (infrared)[°C]	-2.3 ± 1.4	-1.0± 0.8	-0.5 ± 0.6
Humidity[%]	60 ± 7	51 ± 7	68 ± 2
Wind speed [m/s]	2.5 ± 3.0	2.0 ± 2	2.5 ± 1
Wind direction [°]	180.0 ± 81	166 ± 83.0	180. ± 39
Atm. CO_2 conc.[ppm]	400.4 ± 3.3	397.7 ± 3.4	396 ± 3.0
Oceanic CO_2 conc.[ppm]	347.0± 1.6	313.3 ± 26	261.0 ± 7.1

Table 6: Mean values (± standard deviation) of meteorological variables during three different sub-periods of the melt season.

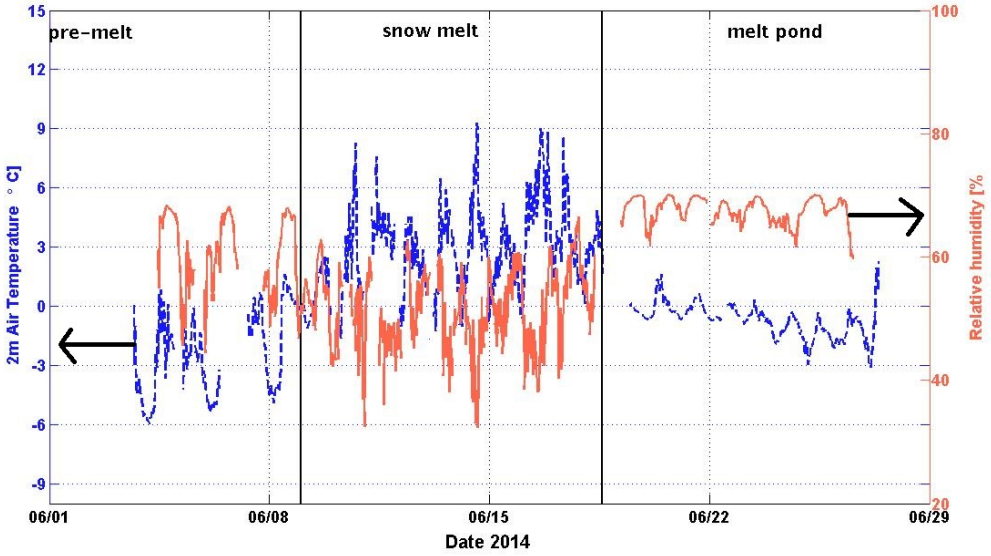

Figure 13: Air temperature (2 m) and relative humidity in Young Sound, June 2014. Solid black lines divide the time series into the three sub-periods, pre-melt, snow melt and melt ponds, discussed in the text.

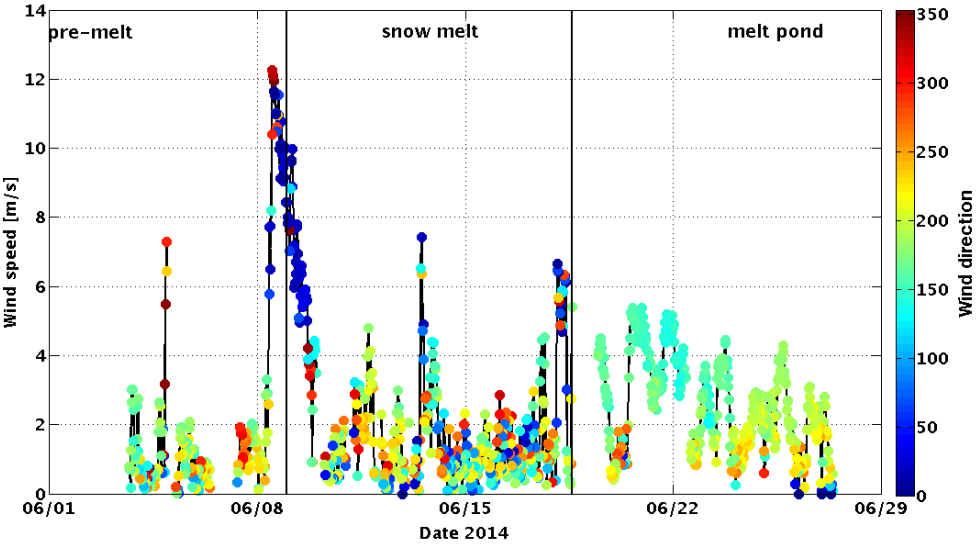

Figure 14: Wind speed and direction in Young Sound June 2014. Wind data is from the weather station data at 3 m. Wind direction is color coded. Solid black lines divide the the time series into the three sub-periods, pre-melt, snow melt and melt pond evolution, discussed in the text.

all ice cores throughout the study. All the ice cores taken during midday and as the air temperature in Figure 13 shows the surface temperature are expected to show

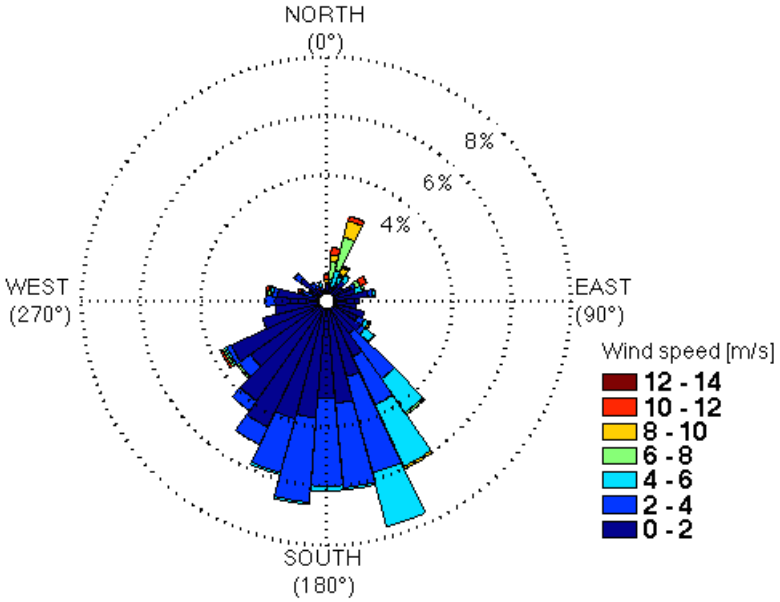

Figure 15: Wind speed and frequency (weather station data) for Young Sound between June 8th and 26th June 2014 from the weather mast data. Directions follow meteorological convention

diurnal variation.

An interesting feature is the big gaps between the ice and snow temperatures at the snow-ice interface, especially early in the season. A possible explanation is sea ice being flushed by sea water under the weight of snow, pushing relatively warm sea water and brine to the top of the ice. Thus, the ice surface and snow bottom temperatures would reflect sea water and atmospheric temperatures respectively, explaining the difference (Nicolas-Xavier Geilfus, personal communication). This idea is supported by the disappearance of the signal with reducing snow cover. Salinity data would confirm this hypothesis.

The only oceanic variable analysed in this work is sea water pCO_2 under ice. The surface water shows a significant decrease in dissolved CO_2(aq) over time. Starting from a steady 347 μatm the concentration dilutes during the snow melt and levels off around 260 μatm at the end of the campaign (Table 6). Given that atmospheric CO_2 concentration are relatively stable, it is this drop in ocean pCO2 that drives the increase in the atmosphere-ocean CO_2 gradient over time shown in

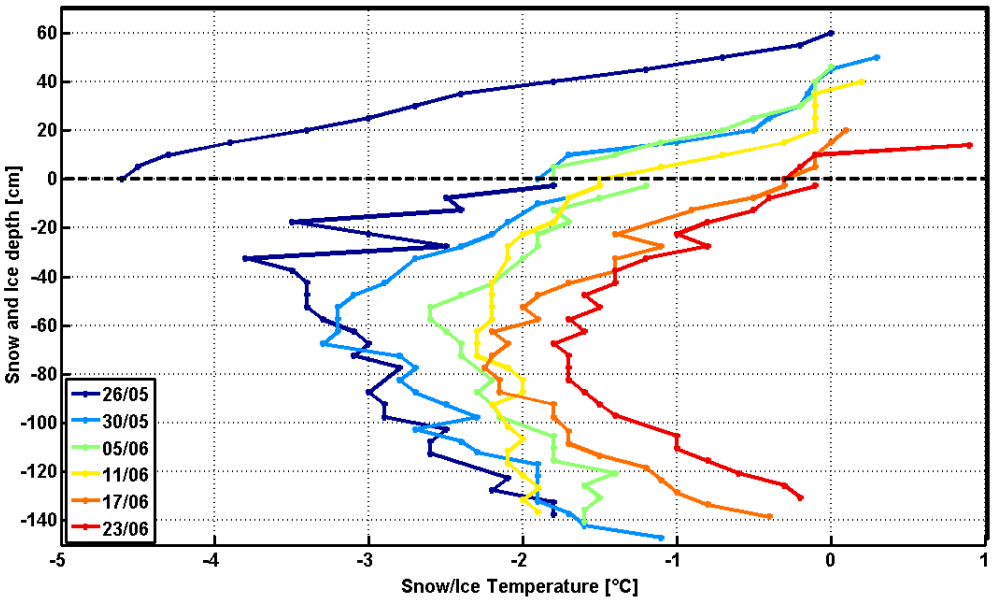

Figure 16: Sea ice and snow temperature profile evolution from ice cores and snow pit measurements. Legend indicates the date when core was extracted.

Figure 19. This gradient increases with almost 100 μatm, from 43 to 140 μatm, in only 10 days demonstrating a significant amplification of the sink potential of the surface waters.

4.2 Surface exchange

Table 7 summarises the surface exchange components for the different subperiods.

4.2.1 Radiation

Table 7 shows that the mean shortwave warming and longwave cooling are strongest during snow melt, 135.4 and -46.3 W/m^2. Both radiative components decrease during the melt pond period. Longwave cooling decreases in proportion more, making the net radiation during melt ponds 5 W/m^2 higher compared to snowmelt.

Despite the midnight sun in Young Sound (74°N), in June, shortwave radiation shows a clear diurnal pattern with the changing insolation angles. The daily maximum shows an increase with the season,in line with the decreasing surface albedo with melt, given clear sky conditions For this time series the maximum was 350 W/m^2 on June 23rd. Clear sky situations are identified with longwave radiative cooling in Figure 17. During the snow melt period the sky was clear with a steady cooling rate of 50 W/m^2. June 16th the cooling steadily diminishes in clear sky

conditions indicating meltpond formation. The surface temperature rises (Equation 3) as all absorbed energy is not used up by phase change. The net radiation oscillates between warming days and cooling nights. During overcast conditions, in the melt pond period, the radiative cooling ceases and the net radiation decreases temporarily (Figure 17). Some clearer days accompanied with longwave loss from the surface are recorded later in the melt pond phase.

4.2.2 Turbulent fluxes

Sensible and latent heat fluxes, calculated with two methods, are plotted in Figure 18. Based on the bulk algorithm the surface was a source of latent heat through out the campaign with increasing energy loss over time. Table 7 shows a bulk algorithm derived mean latent heat flux of 19.2 W/m^2 during the melt pond period. For the EC fluxes the general trend is in line with the bulk algorithm, but the fluxes are generally smaller with an order lower mean cooling rate of 1.3 W/m^2 during the melt pond period. Some negative latent heat fluxes are encountered indicating deposition or condensation of moisture onto the surface. In the pre-melt period the net contribution of turbulent latent heat is close to zero.

For the sensible heat flux the two methods behave somewhat differently. According to the bulk algorithm the sensible heat flux cools the surface during both pre-melt and the melt pond period, but warms it during snowmelt. This is well in line with the observed surface-air temperature gradients (Table 6). The mean turbulent sensible heat flux is slightly negative for all the periods, with a net contribution of practically zero for the melt pond period.

An apparent source of uncertainty is the limited temporal coverage of the turbulent fluxes. This may skew the data, especially if a diurnal cycle goes uncaptured. This applies specifically to the sensible heat flux during the snow melt period, when solar radiation and, thus, temperature showing clear diurnal patterns.

4.2.3 Surface energy budget

Together with the radiative fluxes, the daily net surface energy budget is shown in Figure 17. The net surface energy balance is positive the entire period - translating to surface energy input driving the melt. The highest energy input to the surface is 150 w/m^2 on June 20^{th}.N

The contributions of energy budget components during the different phases of the season are collected in Table 7. As expected, shortwave radiation is the biggest component in the surface energy budget, being balanced by all the resting energy fluxes (Table 7), except sensible heat flux . The bulk algorithm derived mean sensible

Flux [W/m^2]	**Pre-melt**	**Snow melt**	**Melt ponds**
Short-wave rad.	86.7 ± 69.6	135.4 ± 96.9	112.8 ± 90.2
Long-wave rad.	-30.9 ± 20.7	-46.3± 20.3	-18.2 ± 21.6
Net radiation	56.0 ± 63	89.0 ± 95	94.6± 85.1
Latent heat	-0.2± 3.1	0.56 ± 6.4	1.38 ± 5.3
Latent heat(B*)	8.54 ± 9.13	16.37 ± 11.6	19.16 ± 12.8
Sensible heat	0.7 ± 5.1	1 ± 13.3	0.0 ± 3.3
Sensible heat (B*)	-1.2 ± 11.2	11.0 ± 11.3	-9.9 ± 6.9
Conductive heat**	-0.54	0.57	0.15
Net Surf. energy (F_{net})***	70.0 ± 41.0	89.4 ± 17.8	107.6 ± 26
CO_2 flux [μmol/m^{2}s]	-0.06 ± 0.5	-0.18 ± 0.76	0.005 ± 0.4

Table 7: Surface energy budget component mean values (± standard deviation) during three different sub-periods of the melt season. Note! Radiative and conductive fluxes directed toward the surface are positive, whereas turbulent fluxes (Latent heat, sensible heat and CO_2) are negative. *=B denotes bulk fluxes **= no standard deviation given, all values are the mean of two observations(from ice cores). ***= Net surface energy budget (F_{net}) calculated following equation 1. The turbulent fluxes were used for sensible and latent heat.

heat flux contributes with 11 w/m^2 to surface warming during the snow melt. Loss of longwave radiation is the strongest cooling component, especially during pre-melt and snow melt. With the cloudy conditions and a melt pond covered surface the bulk algorithm derived latent heat flux is the largest negative component in the last part of the campaign.

The conductive heat flux is as expected, with melting ice, a very small contribution to the surface energy balance.

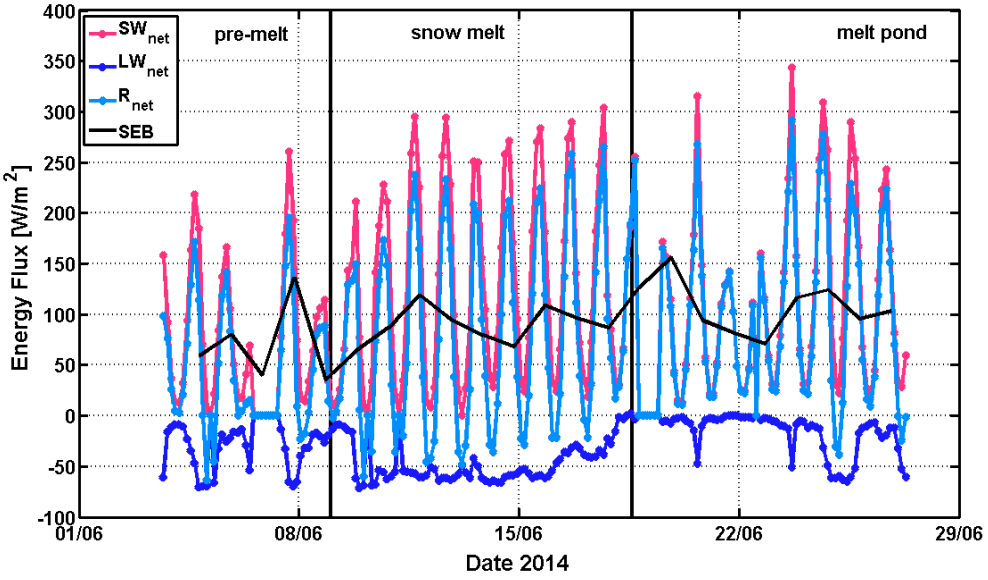

Figure 17: Time series of radiative conditions over sea ice in Young Sounds. SW = shortwave radiation, LW = longwave radiation, R= net radiation(equation 2), F$_{net}$ = surface energy budget at the ice surface calculated according to equation 1.

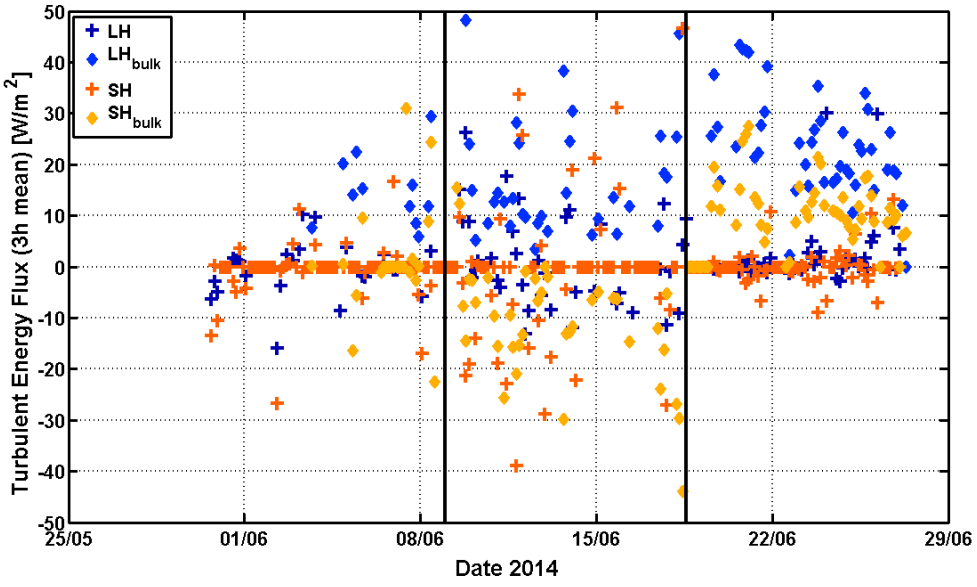

Figure 18: Time series turbulent energy exchange over sea ice in Young Sounds. SH = sensible heat flux, LH = Latent heat flux, X$_{bulk}$ = fluxes calculated with the bulk algorithm (Section 2.3.5).

4.2.4 Atmosphere-surface CO_2 exchange

The measured turbulent air-surface CO_2 exchange ranges between -3.2 and 1.92 μmol/m^{2}s (Figure19).Negative fluxes represent uptake and positive fluxes efflux from the surface. In total 408 flux measurements passed the quality control criteria. The melt pond period is best represented, as low wind speeds, especially during snow melt (Figure 14), reduces significantly the amount of good quality data.

Table 7 shows that the net CO_2 flux was directed into the sea ice during pre melt and snow melt, the uptake being strongest during snow melt. During the melt pond period the flux is in balance, with a net effect close to zero. This is also seen as a flattening of the cumulative flux in Figure 20. Summed over the whole melt season, the ice surface seems to be a net sink for CO_2 in Young Sound (Figure 20). However, the same concern of uneven temporal distribution, as with the sensible heat flux, applies here as well.

Two clear efflux events are visible in Figure 19, June 11^{th} and June 18^{th}. These are the only occasions with effluxes over 1 μmol/m^{2}s. The first efflux event is recorded on June 11^{th}, just at the beginning of the snow melt season in early afternoon. The second efflux event takes place in early morning hours during the transition period from snow melt to melt ponds and follows a very strong uptake (Figure 19). Clear human induced fluxes, such as snow scooters at running at the cite, were cleaned from the data and these events are unconnected to human activities.

4.2.4.1 Diurnal cycle

In Figure 21 the carbon dioxide flux data is divided by the observation hour. For all subperiods the strongest uptake rates (flux $<$ -1μmol/m^{2}s) are observed after local noon. In morning hours(01-10) the uptake being in general smallest. Compared to uptake, the observed efflux is more evenly distributed, the strongest efflux events were observed in the evening, between 16 and 20. Compared to the rest of the time series, the melt pond period shows least variation.

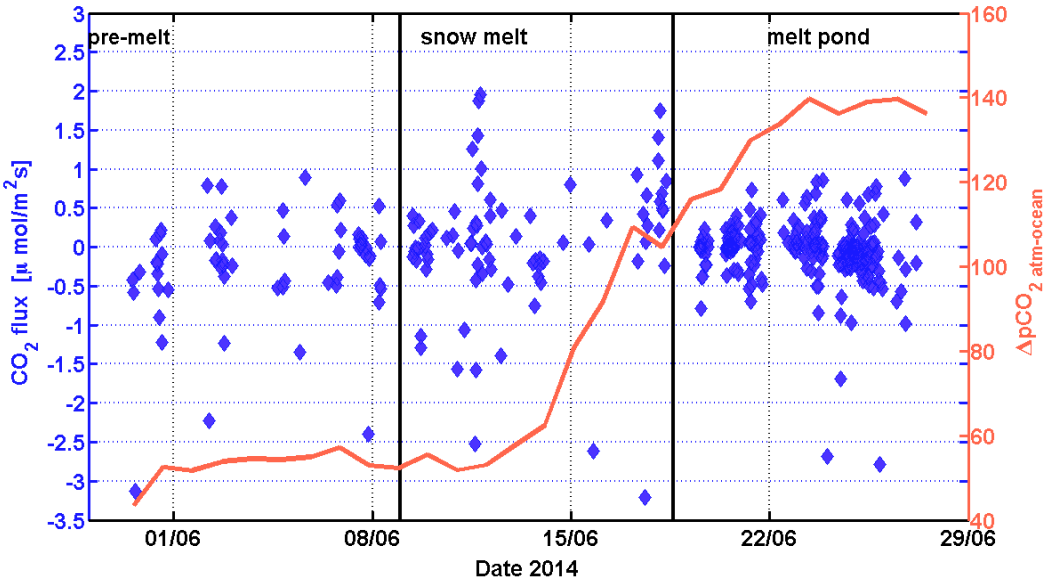

Figure 19: Turbulent CO_2 flux and Atmosphere - Ocean pCO2 gradient in (Positive turbulent CO_2 flux indicates efflux from the ice surface. ΔpCO_2 is positive when the surface waters are a potential sink meaning pCO_2 in the surface water is lower in than in the atmosphere)

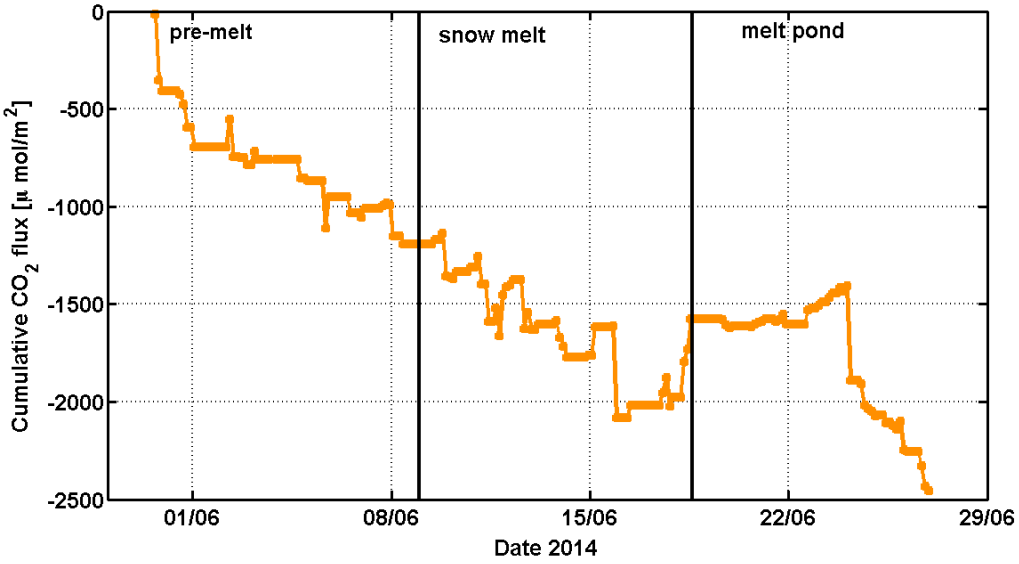

Figure 20: Cumulative sum of turbulent CO_2 flux time series.

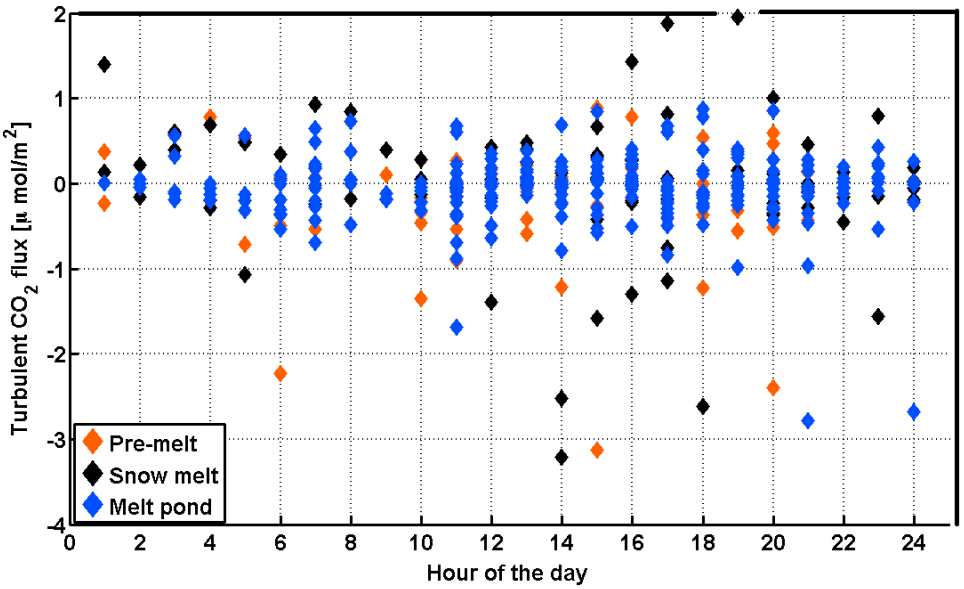

Figure 21: CO_2 exchange for each subperiod sorted by the hour of the day

5 Discussion

5.1 CO_2 exchange

The measured CO_2 fluxes fall in the higher end of the size ranges reported in previous studies. Similar magnitudes are measured with micrometeorological towers in Papakyriakou and Miller (2011), Miller et al. (2011) and Sievers et al. (2015) (see Table 1 in Appendix 1). This study reports the warmest air temperatures for air-ice flux measurements done to date and ice temperatures above the permeability threshold throughout the study. CO_2 exchange is measured throughout the campaign being well in line with previous studies as ice temperatures below -6 to -11 °C are reported to hinder pCO_2 gas exchange(Delille et al., 2014; Geilfus et al., 2012; Papakyriakou and Miller, 2011). The high permeability also supports ocean-atmosphere CO_2 exchange. Several studies encounter a temperature threshold for gas exchange.

An interesting feature in the dataset is the drastic decrease of underwater pCO_2 (Figure 19) observed during the snow melt period. Similar drops in surface water pCO_2 values are captured also in previous studies. Semiletov et al. (2007) reports an undersaturation of 130-150 μatm as a result of a drastic decrease from 410 μatm to 288 μatm in March, in Alaska and Geilfus et al. (2012) reports stable, close to atmospheric, under-ice pCO2 concentrations in April followed by a short period of super saturation (up to 528 μatm) in May followed by a rapid decrease in June, with measurements down to 5 μatm. This drop is accompanied by a freshening of

the under ice water. Both brine and water pCO_2 values drop below the threshold saturation at the same time. Similarly Geilfus et al. (2014) shows a dilution from supersaturation (455 μatm) to undersaturation (259 μatm) and a decrease in salinity between June 7^{th} and June 22^{nd} under Arctic sea ice. is expected to be balanced by an enhanced uptake of atmospheric CO_2. Statistically this cannot be shown from the measurement. At the end of the study the pCO_2 gradient levels off, but a clear oceanic under saturation of 135 ppm remains. It is worth keeping in mind that the oceanic pCO_2 is not measured right under the ice and thus it cannot be expected to be directly connected to the surface exchange.

Previous studies found the air-brine pCO_2 to be the driver of the air - surface CO_2 exchange. Prior melt brine pCO_2 supersaturation is reported in the majority of the studies (Geilfus et al., 2012, 2014; Papakyriakou and Miller, 2011; Miller et al., 2011). In agreement several studies measure effluxes from the ice as the temperature rises above the permeability threshold. As the melt season proceedsGeilfus et al. (2014); Semiletov et al. (2004); Delille et al. (2014); Papakyriakou and Miller (2011) encompass a reversal of the flux , explained with melt water dilution of brine. Geilfus et al. (2012) reports a remarkable drop in brine pCO_2 from 1834 μatm down to almost 0 μatm from early spring to early summer. Similarly, Semiletov et al. (2004) reports significant spring time under saturation, 220-280 μatm in brine pCO_2. In contrast to the rest of studies, in Miller et al. (2011) do not observe a drop in brine pCO_2 and the ice remains a source of CO_2 throughout the melt season. Thus it is expected that if brine pCO2 data were available it could partly explain the miss match between the air-ocean CO_2 gradient and the flux behaviour.

Our dataset is the firs to report EC over fjord ice with fully developed melt ponds. Chamber studies done in Geilfus et al. (2014) report a significant peak in carbon uptake when melt ponds form, but as the melt pond water reaches equilibrium with the atmospheric CO_2 the uptake decreases. Also Chamber measurements by Semiletov et al. (2004) show a tenfold increase in CO_2 uptake with melt pond evolution. Supporting the measurement in Geilfus et al. (2014) we measured the strongest uptake on June 18^{th} when melt ponds were forming, followed by a stabilization of the flux as the surface becomes melt pond covered. We report a zero mean flux during the melt pond phase, whereas Geilfus et al. (2014) shows a moderate net uptake. The decrease in uptake is explained by melt ponds reaching equilibrium with the atmosphere. Our dataset from Young Sound do not include pCO_2 measurements from the melt ponds of our study, but a zero air-meltpond pCO_2 gradient could explain the low exchange rates observed despite the large air-ocean pCO_2 gradient, as the flux is a representation of air-melt pond exchange. In Figure 20 it is clearly visible that as the melt pond period starts, the CO_2 levels of, but after a few days high uptake rates are observed again. This could be an indication of the melt ponds flushing through the ice, allowing for air-ocean CO_2 exchange.

An interesting question is the mechanism causing the surface water pCO_2

decrease. Melt water dilution, increased primary production at the ice bottom, and a decreased alkalinity resulting from dissolution of ice-trapped carbonate salts could all be sea ice related mechanisms leading to a pCO_2 drop. Other, none sea ice related, mechanisms could be the local effect of Zackenberg river discharge. In the melt season the fresh, light, river water could affect the under-ice water properties significantly. However, the river water is expected to have a higher pCO_2 value. The tide is also affecting water masses under the ice in Young Sound. The data presented in this work cannot confirm any of these mechanisms being responsible. However, if the low pCO_2 values are sea ice melt related, then this indicates that sea ice has a strong indirect impact on surface water CO_2 sink strength.

In line with all the previous studies Figure 21 shows that efflux dominates from midnight to 6 am during the melt pond phase, this could indicate that the zero mean flux would be a result of balancing photosynthesis and respiration. Melt pond measurements by Geilfus et al. (2014) do not report any photosynthetic activity in the melt ponds which could possibly explain the different result.

Surface conditions are put forward as the main control of air-ice carbon exchange in all of the previous work. Especially the role of snow is a question arising in the majority of the papers. As confirmed by previous work, (Nomura et al., 2010, 2013), superimposed ice at the surface efficiently blocks the flux. Temperatures below freezing created a crust on the melt ponds during the melt pond period. This may be one reason for the low flux magnitudes recorded between June 19th and June 23rd. We do not expect to measure zero fluxes with the tower instrumentation, as the measurement footprint is affected by open ocean and a polynya in the majority of the measurements.

Unlike Semiletov et al. (2004) we do not find a correlation between wind direction and the flux (not shown). This is assumed to be a reflection of the prevailing conditions. The weak winds and the mainly in-fjord flow, do not give representative data for such an analysis.Papakyriakou and Miller (2011) observes the highest uptake with highest wind speeds. In our study the observed high uptake and low wind speeds are likely a reflection of the wind conditions during the campaign. Based on previously published work, the snow melt period is expected have high uptake rates and this was also the period of very calm winds. Semiletov et al. (2004) detected a connection between airmass origin and carbon exchange. The dataset from 2002 reveals a difference in the temporal trend of the CO_2 flux with wind direction. As the summer proceeds the uptake of CO_2 flux increases with onshore and decreases with offshore winds. The authors suggest that the negative trend found with the onshore winds, originated from the Arctic Ocean, could be explained by ice melt induced uptake of CO_2 as the ice melts and melt ponds develop.On the other hand, increasing primary production depletes CO_2 in air masses travelling across Alaska to Barrow, hence, possibly explaining the opposing trends in the CO_2 flux with different wind directions. It was only the trend that was altered, absolute

values of CO_2 exchange are similar for both onshore and offshore flow.

We do observe a weak negative correlation between the short wave radiation and the net radiation (not shown) indicating surface warming induced uptake. Sievers et al. (2015) reports a stronger correlation with the radiation and, in line with this, an clearer diurnal pattern of night time efflux and daytime uptake. No clear diurnal cycle can be extracted from this data set (Figure 21), but we see a larger deviation in the flux from noon to midnight. A possible explanation for the insignificant correlations could be the state of the ice, all ice cores have temperatures above the permeability threshold (Figure 16). As the ice was relatively warm it will not show an immediate response to radiative cooling. As the night proceeds the surface cools enough to prohibit exchange. This could explain the small uptake rates observed after midnight.

In the snow melt period, with highest energy input, rapid change in the air-ocean pCO_2 gradient and the most pronounced diurnal cycle in both temperature and humidity a high uptake seems to be followed by high efflux. This supports the existence of a diurnal pattern, but also reflect the atmospheric conditions being suitable for good quality measurements. It is unfortunate that the number of good quality observations from the snow melt is very limited, due to under development of turbulence.

Interesting features in the dataset are the two strong efflux events. All observed efflux stronger than 1 μmol/m^{2}s took place between 16 and 02 o'clock, supporting cooling and respiration driven efflux. Wind pumping of the snow pack could also yield in rapid strong efflux events, as the snow deposited CO_2 is released to the atmosphere. In line with the results of Sievers et al. (2015), we observe a positive correlation between wind speed and CO_2 flux. We do not expect to observe as high correlations as Sievers et al. (2015) as we measured over a thinner snow cover and in the last part of the campaign over a melt pond covered surface. Interestingly at winds above 6 m /s almost we see that almost all uptake ceases (not shown). Efflux is observed also in low wind conditions. In general, both magnitude and deviation of the exchange decreases with increasing wind. High winds mix the air effectively, nullifying the vertical CO_2 gradient.During the first efflux event the 4.5 m/s wind was blowing outfjords and the on-ice snow cover was 40cm thick. For this event the wind speed was not extremely high, but the wind was blowing from the fjord. This could be a wind-pumping event, flushing the snow pack. Emission from the Zackenberg reserach station and the thicker snow pack deeper in the fjord could explain the high measurements. In the later event the efflux was recorded in the coldest hours 00-02 with wind from the south and over 6 m/s. The snow cover was clearly melted and was only 20 cm thick. The ice temperature on June 17th is -0.5°C at snow-ice interface. This high flux event could be driven by respiration with warm ice, thin snow and high winds forming good conditions for

air-ice turbulent gas exchange.

All of the discussion above show strong evidence, in agreement with previous studies, that the flux highly dependent of the surface conditions. Further the surface evolution and melt is driven by atmospheric energy input. On a qualitative level this makes a strong link between the surface energy budget and the air-surface CO_2 exchange. However, this dataset is too small to obtain statistically significant results. In addition, previous studies show that many different mechanisms may affect and control the flux and with the data at hand the contribution from these different mechanisms cannot be separated in a trustworthy manner. The energy input shapes all of these mechanisms as both ice permeability and brine carbonate chemistry are functions of temperature and photosynthesis is sunlight driven.

The target of this work was to link surface energy balance and the air-sea ice surface CO_2. Our net energy input at the surface is of similar size to what Else et al. (2014) report from the Canadian Arctic over melting fast-ice. In the melt pond period the energy balance is less representative of the entire surface with the existence of snow and water side by side.The increase in the net shortwave radiation peaks over time (Figure 17) reflects the increased surface absorption. The radiation was measured over snow surface for the whole campaign. If measured over melt ponds the energy input is expected to have increase more during the melt pond period with a lower surface albedo (see Table 1). This work supports the importance of longwave radiation in the melt season found by (Else et al., 2014; Persson, 2012; Maksimovich and Vihma, 2012). The transition to a melt pond covered surface is marked with a net zero longwave radiative balance or, in other words, a thick cloud cover increasing the down welling longwave radiation.

However, the clear disagreement between the EC and bulk algorithm derived fluxes in Figure 18 raises concerns about the quality of the turbulent energy flux data. The eddy covariance method is the direct method to measure and represents an ecosystem scale exchange. However, especially in the melt pond period the measured EC flux is a representation of the whole measurement footprint and this can explain the difference between the Bulk and the EC fluxes. Also the high relative humidities during the melt pond period, may be a source of instrumental uncertainty.

The turbulent fluxes in this data set do not show any significant correlations with the turbulent CO_2 flux (not shown).Sievers et al. (2015) reports an almost perfect correlation with sensible heat flux at the same cite earlier in the season. When the surface is melting the surface temperature remains constant around melting point (indicated by the steady longwave radiative cooling during the snow melt period Figure 13), as the energy exchange drives phase change. Hence the flux is behaving differently in the melt season compared to earlier in the season, explaining the differences in our data set and the one of Sievers et al. (2015).

Based on the temperature time series a clear diurnal pattern in sensible heat flux is expected during the snow melt period.

In similar conditions Else et al. (2013) do not measure any positive latent heat fluxes with eddy covariance instrumentation. Also the bulk algorithm derived fluxes are negative for the complete melt period. With the strong marine input it is not physically impossible to have surface deposition in cold nights. Especially in the snow melt period, when the longwave cooling is constant, sensible and latent heat fluxes show opposite Figure 18 there are periods during melt pond period with negative sensible heat fluxes.

The disagreement of the two conditions raises questions. Eddy covariance methodology is the direct measurement technique and it should be considered as the reference methodology. The reason for the big differences in the bulk and EC fluxes could reflect the constant emissivity value used in for the bulk methodology. This could also be due to uncertainties is the accuracy of the water vapour measurements. The latent heat flux is the only variable depending on the turbulent water vapour measurements.

The coarse resolution of the ice cores lowers the of the conductive heat flux. With in ice temperature thermistors, valuable data of sea ice temperature evolution could be gained. This would probably enable more detailed analysis of the flux behaviour with different ice surface temperatures.

5.2 Measurements

Sea ice is a low flux environment issuing the detection limit of the measurement instrumentation. With low fluxes the noise-to-signal ratio increases. For a eddy covariance system consisting of an open-path gas-analyser and a sonic anemometer similar to Sørensen et al. (2014) the detetction limit over a cotton field is estimated to be 0.02 μmol/ms (Wang et al., 2013). The standard deviation of the measured CO_2 fluxes is big, indicating noise in the measurement system. Both Papakyriakou and Miller (2011) and Else et al. (2011) report sensor heating correction (Burba et al. (2008)) related positive bias. During a low flux period Papakyriakou and Miller (2011) observes overcorrection, the correction component turns low-level uptake to low-level efflux. This arises the question if such small fluxes are above the noise level of the system. Based on testing noise and bias of the eddy covariance system over thick, cold consolidated ice, with expected zero exchange, Else et al. (2011) reports an overall flux uncertainty of 0.77 μmol m^{-2} s^{-1} and a positive bias of +0.13 μmol m^{-2} s^{-1} resulting from the sensor heat correction. A large fraction of the flux measurements reported in this study fall below 0.77 μmol m^{-2} s^{-1}. Of course a one-to-one comparison is not reliable, as instrumental differences are

expected. However the order of magnitude of the uncertainty should be applicable. This suggests that the air-ice flux might be too small to be resolved with our instrumentation. As already mentioned, surface heterogeneity increases with the melt season and makes the tower measurements of both CO_2 and the surface energy budget components less representative for the fjord environment.

All studies done on sea ice have used open-path gas analyzers. The main argument for the usage is the low energy consumption, making field work in harsh Arctic conditions easier. However, the weaknesses with the open-path set-up may have severe consequences on the data quality. One challenge with the open path set up is the sensor self-heating as the instrument lenses are exposed to solar radiation. Previous studies also show that the sensor heating correction goes with a relatively big bias on the flux (Else et al., 2013; Papakyriakou and Miller, 2011). Papakyriakou and Miller (2011) shows that this correction results in a reversed flux direction for some low flux events. In this work we chose not to correct for the self-heating.

The quality criteria applied to the data creates gaps in the time series. Thus the data cannot be analyzed as a complete time series and diurnal variability may be skewed. This lowers the certainty of the cumulative sum. To fill the gaps the drivers of the flux should be known, in order to use independent data for gap filling(Aubinet et al., 2012).

5.2.1 Future studies

Throughout the study the ice temperature is above the permeability threshold and the air-ocean CO_2 gradient An important question being why this data set did not capture a clear sign of equilibration of this air-sea CO_2 gradient. To answer this question the measurement technique should be validated. It is an essential requirement to be confident in the measurements not being a product of a high noise-to-signal ratios.Closed-path flux measurements over sea ice could help overcome the uncertainties related to the open-path instrumentation. Future studies would benefit from a uniform post-processing routine and this would make comparisons more reliable.

This study demonstrates the complexity of the air-ice-ocean environment and for a complete analysis pCO_2 data from both brine and melt ponds should be connected to the surface energy balance and EC CO_2/H_2O measurements.Finally, for a more complete understanding of sea ice induced changes in the Arctic carbon cycling more comparable high quality flux measurements should be conducted in all seasons.

6 Conclusions

This work presents an analysis of surface energy exchange and CO_2 exchange over melting sea ice, collected in over seasonal fast ice in North-East Greenland in June 2014. This work is the first to present Eddy covariance fluxes together with an surface energy balance measurements over a sea ice surface evolving through snow melt to fully developed melt ponds. The study period was divided into three sub periods - pre-melt, snow melt and melt ponds. Ice temperature was above the permeability threshold in Young Sound throughout the campaign, showing a steady warming, and the air-ocean pCO_2 gradient was positive (indicating ocean sink) during the whole measurement campaign.

We measured air CO_2 exchange in the range of -3.2 to 1.9 μ mol / s m^2 (negative fluxes indicating uptake and positive values efflux), comparable to marine and terrestrial exchange rates. These flux magnitudes are in the higher end of the to date reported sea ice surface flux studies. The measured fluxes indicate that sea ice was a net sink of for CO_2 during pre-melt and snow melt periods, during the melt pond period the the net contribution is approximately zero. The net zero flux is suggested to reflect equilibration between atmosphere-melt pond pCO_2 gradient. At the end of the campaign, high uptake rates could signal melt pond flushing through the ice. Similar to previous studies, the highest uptake rates are observed at the end of the snow melt period, just as the melt ponds are formed. The flux shows least deviation in the beginning of the melt pond period with overcast conditions. Two high efflux events were recorded in the time series. The positive correlation found for the wind speed and the CO_2 flux supports wind pumping of snow deposited CO_2 contributing to the surface exchange.

During the melt season the oceanic surface water pCO_2, measured 2.5 m below the ice, decreases with 100 μatm over the course of 10 days, creating a drastic undersaturation of 140 μatm at the end of the campaign. However, the timing of the decrease in the pCO_2 gradient correlates well with the melt period of constant surface temperature, indicating a connection between the increased sink potential and sea ice melt. This is a strong support for sea ice being an active component in the carbon cycling in Young Sound.

The net surface energy budget is found to be positive during the entire study, indicating melt, and as expected net shortwave radiation is the biggest component of the net energy flux. Net short wave radiation increases with the season, given clear sky conditions, in line with the decreasing surface albedo. At the start of the melt pond period thick clouds hinder longwave radiative loss creating a peak in the net surface energy budget.

The turbulent heat fluxes are an order of smaller compared to the net radiation.

The Eddy Covariance fluxes of latent and sensible heat fluxes were almost in balance during the whole campaign, only after melt ponds were formed was the latent heat flux cooling the surface through evaporation, as expected. The bulk algorithm fluxes, based on weather station measurements, suggests that the surface was a heat source during pre-melt and melt pond periods, but a sink during the snow melt period as a result of the constant surface temperature. The bulk algorithm derived latent heat flux indicates the surface being a source of vapour, cooling the surface during the entire campaign. The reliability of the turbulent fluxes is questioned as the methods disagree.

This study did not find as strong correlations between the CO_2 exchange and the surface energy budget as previous studies by (Sievers et al., 2015) done earlier in the season in the same fjord. However this data shows a weak correlation between net radiation and the sensible heat flux, as expected. Both of these correlations support the flux being controlled by the surface conditions and indicates the existence of a diurnal cycle. The dissimilarities between our study and Sievers et al. (2015), especially for the sensible heat flux, were explained by the close to constant surface temperature during the melt season.

The study was conducted with two masts with a sonic anemometer and an open-path gas-analyser at a height approximately 3 m. A big part of the turbulence data was discarded due to strict quality criteria. This demonstrated the challenge of measuring high quality fluxes in remote conditions and low flux environments. In this work we also raise the question of applicability of open-path gas analyser measurements in Arctic conditions, over sea ice. Majority of the reported fluxes are below the certainty threshold reported for similar instrument set up (Else et al., 2013). Another important issue arising from this data is the large uncertainties with the post processing corrections connected with the open-path gas analyser. We suggest closed-path infra-red gas-analysers should be used to validate the observed fluxes over sea ice. Considering future research an appropriate gap-filling method should be applied in order to resolve hourly, monthly and further yearly averages. Further, it is evident that the understanding and quantifying net contribution of the sea ice cycle on the carbon balance requires continuous measurements from all seasons.

All in all, this study supports of the conceptual model of sea ice melt being a pump mechanism of CO_2 into the Arctic waters. The cumulative sum of the good quality fluxes indicates Young Sound fjord ice being a net sink of CO_2. This study is the first connecting micrometeorological flux measurements of CO_2 together with surface energy balance components. However, this data set is by itself not strong enough to conclude statistically significant correlations, as the prevailing wind conditions and strict quality criteria creates gaps in the data set and reduces the amount of good quality measurements. For future work this data should be utilized in addition with other ice flux datasets to strengthen the

understanding of specific drivers and controls of ice-atmosphere CO_2 exchange. Despite the uncertainties, this data set suggests a strong impact of melt ponds on both sea ice surface energy balance and the CO_2 exchange, in line with Geilfus et al. (2013), and more melt pond formation specific studies would be needed to further study this. In general, more good quality data and alternative measurement strategies are needed to confirm our results and to quantify the sea ice melt season carbon exchange. As a final conclusion, this data set strongly motivates future studies on sea ice melt induced changes in the carbon cycling in Arctic waters.

Acknowledgements

This work was done at the Finnish Metorological Institute in the group of *Polar Meteorology and Climatology*. I wish to express my sincere thanks to my supervisor in Helsinki Dos. Timo Vihma for all support and guidance with my work. I am also very grateful to my other supervisor Prof. Tim Papakyriakou from Universty of Manitoba, who made this project possible and was supervising my field work in Greenland. A special thanks goes also to Prof. Lise-Lotte Sørensen from Aarhus University for valuable help with the data processing and interpretation.

The field work in Young Sound, Greenland made the heart of this thesis and it was a great experience for me. I take this opportunity to express gratitude to all the people working with me on the fjord ice during Leg 3 of the 2014 Young Sound campaign, especially the Arctic Science Partnership (ASP) logistics. I also gratefully acknowledge the contributions of the Academy of Finland, the Canada Excellence Research Chair (CERC) , Canada Research Chair (CRC) programs, Natural Sciences and Engineering Research (NSERC) Council, the Canada Foundation for Innovation , University of Manitoba for funding this work. The 2014 Young Sound- field campaign was a contribution to the ArcticNet Networks of Centres of Excellence and the Arctic Science Partnership (ASP).

Bibliography

Aagaard, K. and E. C. Carmack, 1989: The role of sea ice and other fresh water in the arctic circulation. *Journal of Geophysical Research: Oceans*, **94**(C10), 14485–14498.

American Meteorological Society, 2014: Reynolds stress. *Glossary of Meteorology [Available online at http://glossary.ametsoc.org/wiki/reynolds]*. Cited 02/14.

Andreas, E. L., 2002: Parameterizing scalar transfer over snow and ice: A review. *Journal of Hyhdrometeorology*, **3**(4), 417–432.

Andreas, E. L., P. O. G. Persson, A. A. Grachev, R. E. Jordan, T. W. Horst, P. S. Guest and C. W. Fairall, 2010: Parameterizing turbulent exchange over sea ice in winter. *J. Hydrometeor*, **11**, 87–104.

Arrigo, K., D. Robinson, D. Worthen, R. Dunbar, G. Di Tullio, M. Van Woert and M. Lizotte, 1999: Phytoplankton community structure and the drawdown of nutrients and co_2 in the southern ocean. *Science*, **283**, 365–367.

Arrigo, K. R., S. Pabi, G. L. van Dijken and W. Maslowski, 2010: Air-sea flux of co_2 in the arctic ocean, 1998 − 2003. *Journal of Geophysical Research: Biogeosciences*, **115**(G4).

Aubinet, M., T. Vesala and D. Papale, 2012: *Eddy Covariance - A Practical Guide to Measurement and Data Analysis*. Springer Netherlands.

Bates, N. R. and J. T. Mathis, 2009: The arctic ocean marine carbon cycle: evaluation of air-sea co_2 exchanges, ocean acidification impacts and potential feedbacks. *Biogeosciences*, **6**(11), 2433–2459.

Bhatt, U. S., D. A. Walker, M. K. Raynolds, J. C. Comiso, H. E. Epstein, G. Jia, R. Gens, J. E. Pinzon, C. J. Tucker, C. E. Tweedie et al., 2010: Circumpolar arctic tundra vegetation change is linked to sea ice decline. *Earth Interactions*, **14**(8), 1–20.

Blunden, J. and D. Arndt, 2012: State of the climate in 2011. *Bull. Am. Meteorol. Soc.*, **93**. Special supplement.

Burba, G. G., D. K. Mcdermitt, A. Grelle, D. J. Anderson and L. Xu, 2008: Addressing the influence of instrument surface heat exchange on the measurements of co_2 flux from open-path gas analyzers. *Global Change Biology*, **14**(8), 1854–1876.

Cavalieri, D. J. and C. L. Parkinson, 2012: Arctic sea ice variability and trends, 1979ndash;2010. *The Cryosphere*, **6**(4), 881–889.

Ciais, P., C. Sabine, G. Bala, L. Bopp, V. Brovkin, J. Canadell, A. Chhabra, R. DeFries, J. Galloway, C. Heimann, M.and Jones, C. Le Quéré, R. Myneni, P. S. and P. Thornton, 2013: Carbon and other biogeochemical cycles. Teoksessa: *Climate Change 2013: The Physical Science Basis. Contribution of Working Group I to the Fifth Assessment Report of the Intergovernmental Panel on Climate Change* (toimittanut Stocker, T., D. Qin, G.-K. Plattner, M. Tignor, S. Allen, J. Boschung, A. Nauels, Y. Xia, V. Bex and P. e. Midgley). Cambridge University Press, Cambridge, United Kingdom and New York, NY, USA.

Comiso, J. C. and F. Nishio, 2008: Trends in the sea ice cover using enhanced and compatible amsr-e, ssm/i, and smmr data. *Journal of Geophysical Research: Oceans*, **113**(C2). C02S07.

Delille, B., M. Vancoppenolle, N.-X. Geilfus, B. Tilbrook, D. Lannuzel, V. Schoemann, S. Becquevort, G. Carnat, D. Delille, C. Lancelot et al., 2014: Southern ocean co_2 sink: The contribution of the sea ice. *Journal of Geophysical Research: Oceans*, **119**(9), 6340–6355.

Deser, C., R. Tomas, M. Alexander and D. Lawrence, 2010: The seasonal atmospheric response to projected arctic sea ice loss in the late twenty-first century. *Journal of Climate*, **23**(2), 333–351.

Dieckmann, G., G. Nehrke, C. Uhlig, J. Göttlicher, S. Gerland, M. Granskog and D. Thomas, 2010: Ikaite (caco3. $6h_2o$) discovered in arctic sea ice. *The Cryosphere*, **4**, 227–230.

Dieckmann, G. S., G. Nehrke, S. Papadimitriou, J. Göttlicher, R. Steininger, H. Kennedy, D. Wolf-Gladrow and D. N. Thomas, 2008: Calcium carbonate as ikaite crystals in antarctic sea ice. *Geophysical Research Letters*, **35**(8).

Eicken, H., H. R. Krouse, D. Kadko and D. K. Perovich, 2002: Tracer studies of pathways and rates of meltwater transport through arctic summer sea ice. *Journal of Geophysical Research:*

Oceans, **107**(C10), SHE 22–1–SHE 22–20.

Else, B. G. T., T. N. Papakyriakou, R. J. Galley, W. M. Drennan, L. A. Miller and H. Thomas, 2011: Wintertime co2 fluxes in an arctic polynya using eddy covariance: Evidence for enhanced air-sea gas transfer during ice formation. *Journal of Geophysical Research: Oceans*, **116**(C9), n/a–n/a.

Else, B. G. T., R. J. Galley, B. Lansard, D. G. Barber, K. Brown, L. A. Miller, A. Mucci, T. N. Papakyriakou, J. Tremblay and S. Rysgaard, 2013: Further observations of a decreasing atmospheric co_2 uptake capacity in the canada basin (arctic ocean) due to sea ice loss. *Geophys. Res.Lett.*, **40**.

Else, B. G. T., T. N. Papakyriakou, R. Raddatz, C. J. Mundy, D. Barber, K. Swystun and S. Rysgaard, 2014: Surface energy bubget of landfast sea ice during the transition from winter snowmelt and melt pond onset: The importance of net longwave radiation and cyclone forcings. *Journal of Geophysical Research: Oceans*.

Esau, I. and S. Zilitinkevich, 2010: On the role of the planetary boundary layer depth in the climate system. *Advances in Science and Research*, **4**(1), 63–69.

Finnigan, J., 2004: A re-evaluation of long-term flux measurement techniques part ii: coordinate systems. *Boundary-Layer Meteorology*, **113**(1), 1–41.

Flocco, D., D. Schroeder, D. L. Feltham and E. C. Hunke, 2012: Impact of melt ponds on arctic sea ice simulations from 1990 to 2007. *Journal of Geophysical Research: Oceans (1978–2012)*, **117**(C9).

Geilfus, N. X., G. Carnat, T. Papakyriakou, J. L. Tison, T. H. Else, B., E. Shadwick and B. Delille, 2012: Dynamics of pco_2 and related air-ice co_2 fluxes in the arctic coastal zone (amundsen gulf, beaufort sea). *J. Geophys. Res. Ocean.*, **117**.

Geilfus, N.-X., G. Carnat, G. S. Dieckmann, N. Halden, G. Nehrke, T. Papakyriakou, J.-L. Tison and B. Delille, 2013: First estimates of the contribution of caco3 precipitation to the release of co2 to the atmosphere during young sea ice growth. *Journal of Geophysical Research: Oceans*, **118**(1), 244–255.

Geilfus, N.-X., R. Galley, O. Crabeck, T. Papakyriakou, J. Landy, J.-L. Tison and S. Rysgaard, 2014: Inorganic carbon dynamics of melt pond-covered first year sea ice in the canadian arctic. *Biogeosciences Discussions*, **11**, 7485–7519.

Gleitz, M., M. R. Loeff, D. N. Thomas, G. S. Dieckmann and F. J. Millero, 1995: Comparison of summer and winter inorganic carbon, oxygen and nutrient concentrations in antarctic sea ice brine. *Marine Chemistry*, **51**(2), 81–91.

Golden, K. M., H. Eicken, A. L. Heaton, J. Miner, D. J. Pringle and J. Zhu, 2007: Thermal evolution of permeability and microstructure in sea ice. *Geophysical Research Letters*, **34**(16).

Gosink, T. A., J. G. Pearson and J. J. Kelley, 1976: Gas movement through sea ice,. *Nature*, **263**, 41–42.

Haslwanter, A., A. Hammerle and G. Wohlfahrt, 2009: Open-path vs. closed-path eddy covariance measurements of the net ecosystem carbon dioxide and water vapour exchange: A long-term perspective. *Agricultural and Forest Meteorology*, **149**(2), 291 – 302.

Holton, J., 2004: *An Introduction to Dynamic Meteorology*. No. 1. Elsevier Academic Press. ISBN 9780123540157.

Jones, E., A. Coote and E. Levy, 1983: Effect of sea ice meltwater on the alkalinity of seawater. *Journal of Marine Research*, **41**(1), 43–52.

Kaimal, J. C. and J. J. Finnigan, 1994: Atmospheric boundary layer flows: their structure and measurement.

Kelley, J., 1987: Carbon dioxide in the arctic environment. *The Journal of Earth Sciences*, **35**, 341–354.

Kwok, R., G. Cunningham, M. Wensnahan, I. Rigor, H. Zwally and D. Yi, 2009: Thinning and volume loss of the arctic ocean sea ice cover: 2003–2008. *Journal of Geophysical Research: Oceans (1978–2012)*, **114**(C7).

Liu, H., G. Peters and T. Foken, 2001: New equations for sonic temperature variance and buoyancy heat flux with an omnidirectional sonic anemometer. *Boundary-Layer Meteorology*, **100**(3), 459–

468.

Loose, B., A. Miller, L, S. Elliott and T. Papakyriakou, 2011: Sea ice biogeochemistry and material transport across the frozen interface. *Ocean*, **24**.

Lund, M., J. M. Falk, T. Friborg, H. N. Mbufong, C. Sigsgaard, H. Soegaard and M. P. Tamstorf, 2012: Trends in co_2 exchange in a high arctic tundra heath, $2000 - 2010$. *Journal of Geophysical Research: Biogeosciences*, **117**(G2).

Maksimovich, E. and T. Vihma, 2012: The effect of surface heat fluxes on interannual variability in the spring onset of snow melt in the central arctic ocean. *Journal of Geophysical Research: Oceans*, **117**(C7), n/a–n/a.

Markus, T., J. C. Stroeve and J. Miller, 2009: Recent changes in arctic sea ice melt onset, freezeup, and melt season length. *Journal of Geophysical Research: Oceans (1978–2012)*, **114**(C12).

Mauder, M., S. P. Oncley, R. Vogt, T. Weidinger, B. C. Ribeiro, L., T. Foken, W. Kohsiek, H. A. R. De Bruin and H. Liu, 2007: The energy balance experiment ebex-2000, part ii: Intercomparison of eddy-covariance sensors and post-field data processing methods. *Bound.-Lay. Meteorol.*, **123**, 29–53.

McMillen, R., 1988: An eddy correlation technique with extended applicability to non-simple terrain. *Boundary-Layer Meteorology*, **43**(3), 231–245.

Miller, L. A., T. N. Papakyriakou, R. E. Collins, J. W. Deming, J. K. Ehn, R. W. Macdonald, A. Mucci, O. Owens, M. Raudsepp and N. Sutherland, 2011: Carbon dynamics in sea ice: A winter flux time series. *Journal of Geophysical Research: Oceans*, **116**(C2).

Montgomery, R. B., 1948: Vertical eddy flux of heat in the atmosphere. *J. Meteorol.*, **5**, 265â274.

Nomura, D., H. Yoshikawa-Inoue and T. Toyota, 2006: The effect of sea-ice growth on air-sea co_2flux in a tank experiment. *Tellus B Chem. Phys. Meteorol.*, **58**, 418–426.

Nomura, D., H. Yoshikawa-Inoue, T. Toyota and K. Shirasawa, 2010: Effects of snow, snowmelting and refreezing processes on airâsea-ice co_2 flux. *Journal of Glaciology*, **56**(196).

Nomura, D., M. A. Granskog, P. Assmy, D. Simizu and G. Hashida, 2013: Arctic and antarctic sea ice acts as a sink for atmospheric co2 during periods of snowmelt and surface flooding. *Journal of Geophysical Research: Oceans*, **118**(12), 6511–6524.

Notz, D. and M. G. Worster, 2009: Desalination processes of sea ice revisited. *Journal of Geophysical Research: Oceans (1978–2012)*, **114**(C5).

Notz, D., M. G. McPhee, M. G. Worster, G. A. Maykut, K. H. SchlÃ$\frac{1}{4}$nzen and H. Eicken, 2003: Impact of underwater-ice evolution on arctic summer sea ice. *Journal of Geophysical Research: Oceans*, **108**(C7).

Obukhov, A. M., 1951: Charakteristiki mikrostruktury vetra v prizemnom sloje atmosfery (characteristics of the micro-structure of the wind in the surface layer of the atmo- sphere). *Izv. AN SSSR, ser. Geofiz.*, **3**, 49–68.

Oke, T. R., 1987: *Boundary layer climates*. Routledge, 1. painos.

Overland, J., M. Wang, J. Walsh, J. Christensen, V. Kattsov and W. Chapman, 2011: Chapter 3: Climate model projections for the arctic. Teoksessa: *In Snow, Water, Ice and Permafrost in the Arctic (SWIPA)*. Arctic Monitoring and Assessment Programme (AMAP).

Papakyriakou, T. and L. Miller, 2011: Springtime co_2 exchange over seasonal sea ice in the canadian arctic archipelago. *Ann.glaciol*, **52**.

Parmentier, F. J. W., M. K. van der Molen, J. van Huissteden, S. A. Karsanaev, A. V. Kononov, D. A. Suzdalov, T. C. Maximov and A. J. Dolman, 2011: Longer growing seasons do not increase net carbon uptake in the northeastern siberian tundra. *Journal of Geophysical Research: Biogeosciences*, **116**(G4).

Parmentier, F.-J. W., T. R. Christensen, L. L. Sørensen, S. Rysgaard, A. D. McGuire, P. A. Miller and D. A. Walker, 2013: The impact of lower sea-ice extent on arctic greenhouse-gas exchange. *Nature climate change*, **3**(3), 195–202.

Perovich, D. K. and C. Polashenski, 2012: Albedo evolution of seasonal arctic sea ice. *Geophysical Research Letters*, **39**(8). L08501.

Persson, P. O. G., 2012: Onset and end of the summer melt season over sea ice: thermal structure and surface energy perspective from sheba. *Climate dynamics*, **39**(6), 1349–1371.

Persson, P. O. G., C. W. Fairall, E. L. Andreas, P. S. Guest and D. K. Perovich, 2002: Measurements near the atmospheric surface flux group tower at sheba: Near-surface conditions and surface energy budget. *Journal of Geophysical Research: Oceans*, **107**(C10).

Pringle, D., J. Miner, H. Eicken and K. Golden, 2009: Pore space percolation in sea ice single crystals. *Journal of Geophysical Research: Oceans (1978–2012)*, **114**(C12).

Rysgaard, S. and R. N. Glud, 2007: Carbon cycling in arctic marine ecosystems: Case study young sound. *Bioscience*, **58**.

Rysgaard, S., R. N. Glud, M. K. Sejr, J. Bendtsen and P. B. Christensen, 2007: Inorganic carbon transport during sea ice growth and decay: a carbon pump in polar seas. *J. Geophys. Res.*, **112**.

Rysgaard, S., J. Bendtsen, L. T. Pedersen, H. Ramløv and R. N. Glud, 2009: Increased co_2 uptake due to sea ice growth and decay in the nordic seas. *Journal of Geophysical Research: Oceans*, **114**(C9).

Rysgaard, S., J. Bendtsen, B. Delille, G. S. Dieckmann, K. H. Glud, R. N., J. Mortensen, S. Papadimitriou, D. N. Thomas and J. L. Tison, 2011: Sea ice contribution to the airâsea co_2 exchange in the arctic and southern oceans. *Tellus B*, **63**, 823–830.

Rysgaard, S., R. N. Glud, K. Lennert, M. Cooper, L. R. J. G. Halden, N., F. C. Hawthorne and D. Barber, 2012: Ikaite crystals in melting sea ice â implications for pco_2 and ph levels in arctic surface waters. *The Cryosphere*, **6**, 901–908.

Rysgaard, S., F. Wang, R. J. Galley, R. Grimm, M. Lemes, N.-X. Geilfus, A. Chaulk, A. A. Hare, O. Crabeck, B. G. T. Else, K. Campbell, T. Papakyriakou, L. L. Sørensen, J. Sievers and D. Notz, 2013: Dynamic ikaite production and dissolution in sea ice - control by temperature, salinity and pCO_2 conditions. *The Cryosphere Discussions*, **7**, 6075–6099.

Rysgaard, S., F. Wang, R. J. Galley, R. Grimm, D. Notz, M. Lemes, N.-X. Geilfus, A. Chaulk, A. A. Hare, O. Crabeck, B. G. T. Else, K. Campbell, L. L. Sørensen, J. Sievers and T. Papakyriakou, 2014: Temporal dynamics of ikaite in experimental sea ice. *The Cryosphere*, **8**(4), 1469–1478.

Sahlée, E., A.-S. Smedman, A. Rutgersson and U. Höogström, 2008: Spectra of co_2 and water vapour in the marine atmospheric surface layer. *Boundary-Layer Meteorology*, **126**(2), 279–295.

Savijärvi, H. and T. Vihma, 2001: *Rajakerroksen Fysiikka 1*.

Screen, J. A. and I. Simmonds, 2010: The central role of diminishing sea ice in recent arctic temperature amplification. *Nature*, **464**(7293), 1334–1337.

Screen, J. A. and I. Simmonds, 2012: Declining summer snowfall in the arctic: Causes, impacts and feedbacks. *Climate dynamics*, **38**(11-12), 2243–2256.

Screen, J. A., I. Simmonds, C. Deser and R. Tomas, 2013: The atmospheric response to three decades of observed arctic sea ice loss. *Journal of Climate*, **26**(4), 1230–1248.

Sejr, M. K., D. Krause-Jensen, S. Rysgaard, L. L. Sørensen, P. B. Christensen and R. N. Glud, 2011: Air–sea flux of co_2 in arctic coastal waters influenced by glacial melt water and sea ice. *Tellus B*, **63**(5), 815–822.

Semiletov, I., A. Makshtas, S.-I. Akasofu and E. L Andreas, 2004: Atmospheric co_2 balance: The role of arctic sea ice. *Geophysical Research Letters*, **31**(5).

Semiletov, I. P., I. I. Pipko, I. Repina and N. E. Shakhova, 2007: Carbonate chemistry dynamics and carbon dioxide fluxes across the atmosphere–ice–water interfaces in the arctic ocean: Pacific sector of the arctic. *Journal of Marine Systems*, **66**(1), 204–226.

Serreze, M. C. and R. B. Barry, 2005a: *The Arctic Climate System*, luku 5. Cambridge University Press.

Serreze, M. C. and R. B. Barry, 2005b: *The Arctic Climate System*, luku 2. Cambridge University Press.

Serreze, M. C. and R. B. Barry, 2005c: *The Arctic Climate System*, luku 6. Cambridge University Press.

Sievers, J., L. L. Sørensen, T. Papakyriakou, M. K. Sejr, D. H. Søgaard, D. Barber and S. Rysgaard, 2015: Winter observations of co_2 exchange between sea-ice and the atmosphere in a coastal fjord environment. *The Cryosphere Discussions*, **9**(1), 45–75.

Sigman, D. M., M. P. Hain and G. H. Haug, 2010: The polar ocean and glacial cycles in atmospheric co2 concentration. *Nature*, **466**(7302), 47–55.

Skogseth, R., P. M. Haugan and J. Haarpaintner, 2004: Ice and brine production in storfjorden from four winters of satellite and in situ observations and modeling. *Journal of Geophysical Research: Oceans*, **109**(C10), n/a–n/a.

Sørensen, L. L., B. Jensen, R. N. Glud, D. F. McGinnis, M. K. Sejr, J. Sievers, D. H. Søgaard, J.-L. Tison and S. Rysgaard, 2014: Parameterization of atmosphereâsurface exchange of co_2 over sea ice. *The Cryosphere*, **8**(3), 853–866.

Stammerjohn, S., R. Massom, D. Rind and D. Martinson, 2012: Regions of rapid sea ice change: An inter-hemispheric seasonal comparison. *Geophysical Research Letters*, **39**(6), n/a–n/a.

Stroeve, J. C., M. C. Serreze, M. M. Holland, J. E. Kay, J. Malanik and A. P. Barrett, 2012: The arcticâs rapidly shrinking sea ice cover: a research synthesis. *Climatic Change*, **110**(3-4), 1005–1027.

Stull, R. B., 1988: *An introduction to boundary layer meteorology*. Springer Science & Business Media.

Sturm, M., J. Holmgren and D. K. Perovich, 2002: Winter snow cover on the sea ice of the arctic ocean at the surface heat budget of the arctic ocean (sheba): Temporal evolution and spatial variability. *Journal of Geophysical Research: Oceans*, **107**(C10), SHE 23–1–SHE 23–17.

Swinbank, W. C., 1951: The measurement of vertical transfer of heat and water vapor by eddies in the lower atmosphere. *J. Meteorol.*, **8**, 135–145.

Takahashi, S. C., T.and Sutherland, C. Sweeney, A. Poisson, T. B. Metzl, N., N. Bates, R. Wanninkhof, R. A. Feely, C. Sabine, J. Olafsson and Nojiri, 2002: Global sea-air co_2 flux based on climatological surface ocean pco_2 and seasonal biological and temperature effects. *Deep-Sea Res. II Top. Stud. Oceanogr*, **47**, 1601â1622.

Takahashi, T., J. Olafsson, J. G. Goddard, D. W. Chipman and S. Sutherland, 1993: Seasonal variation of co_2 and nutrients in the high-latitude surface oceans: A comparative study. *Global Biogeochemical Cycles*, **7**(4), 843–878.

Takahashi, T., C. Sweeney, B. Hales, D. Chipman, T. Newberger, J. Goddard, R. Iannuzzi and S. Sutherland, 2012: The changing carbon cycle in the southern ocean. *Oceanography*, **25**.

Tison, J.-L., C. Haas, M. M. Gowing, S. Sleewaegen and A. Bernard, 2002: Tank study of physico-chemical controls on gas content and composition during growth of young sea ice. *Journal of Glaciology*, **48**(161).

Toggweiler, J. R., A. Gnanadesikan, S. Carson, R. Murnane and J. L. Sarmiento, 2003: Representation of the carbon cycle in box models and gcms: 1. solubility pump. *Global Biogeochemical Cycles*, **17**(1), n/a–n/a. 1026.

Vickers, D. and L. Mahrt, 1997: Quality control and flux sampling problems for tower and aircraft data. *Journal of Atmospheric and Oceanic Technology*, **14**.

Vihma, T., R. Pirazzini, I. Fer, I. A. Renfrew, J. Sedlar, M. Tjernström, C. Lüpkes, T. Nygård, D. Notz, J. Weiss, D. Marsan, B. Cheng, G. Birnbaum, S. Gerland, D. Chechin and J. C. Gascard, 2014: Advances in understanding and parameterization of small-scale physical processes in the marine arctic climate system: a review. *Atmospheric Chemistry and Physics*, **14**(17), 9403–9450.

Wang, K., C. Liu, X. Zheng, M. Pihlatie, B. Li, S. Haapanala, T. Vesala, H. Liu, Y. Wang, G. Liu and F. Hu, 2013: Comparison between eddy covariance and automatic chamber techniques for measuring net ecosystem exchange of carbon dioxide in cotton and wheat fields. *Biogeosciences*, **10**(11), 6865–6877.

Warren, S. G., 1982: Optical properties of snow. *Reviews of Geophysics*, **20**(1), 67–89.

Webb, E. K., G. I. Pearman and R. Leuning, 1980: Correction of flux measurements for density effects due to heat and water vapour transfer. *Quarterly Journal of the Royal Meteorological Society*, **106**(447), 85–100.

Zemmelink, H. J., B. Delille, J. L. Tison, E. J. Hintsa, L. Houghton and J. W. H. Dacey, 2006: Co2 deposition over the multi-year ice of the western weddell sea. *Geophysical Research Letters*, **33**(13).

Appendix A

Summary of previous studies

Table 8: **Summary of previous Eddy Covariance CO_2 flux measurements over sea ice. Abbreviations: *CA* = Canadian Arctic, *NE* = North-East, *SW* = South-West** *Cite was located on Young Sound fjord ice, very close to the measurement cite of this study

Published study	Time (month/year), measurement cite	Flux range (mean)[μmol/m^{2}s]	Surface description
Papakyriakou and Miller (2011)	05/02-06/02, CA	-3 to 1	1^{st} year fast ice
Semiletov et al. (2004)	06/02, Alaska	-0.8 to 0.6	1^{st} year fast ice
Miller et al. (2011)	01/04-06/04, CA	-0.7 to 1 (0.86)	Growing fast ice
Zemmelink et al. (2006)	12/04, Antarctica	-0.2 to -0.05 (-0.16)	Multi year ice
Semiletov et al. (2007)	09/07, Laptev Sea	-0.04 to 0.005	Drifting ice station
Else et al. (2011)**	11/07-01/08, Amundsen Gulf CA	-27.95 to 2.10 (-4.88)	Polynya region
		-0.42 to 0.23	1^{st} year fast ice
Sørensen et al. (2014)	03/10, SW Greenland	-0.34 to 0.43	1^{st} year fast ice
Sievers et al. (2015)	03/12-04/12,Young Sound NE Greenland	-1 to 3 (0.2)	1^{st} year fast ice (cite 1*)
		-0.25 to 0.19 (0.01)	1^{st} year fast ice (cite 2)
		-0.82 to 0.82 (0.2)	Polynya region

Table 9: **Summary of previous chamber measurements of CO_2 fluxover sea ice. Abbreviations: *CA* = Canadian Arctic**

Published study	Time (month/year), measurement cite	Flux range (mean)[μmol/m$^3 s$]	Surface description
Semiletov et al. (2004)	06/02, Alaska	-0.01 to -8*10^{-4}	1^{st} year fast ice with melt ponds
Delille et al. (2014)	09/03-10/03,11/04-12/05 and 10/07, Antarctica	-0.06 to 0.02	1^{st} year and multi-year pack ice
Geilfus et al. (2012)	04/08-06/08 CA	-0.03 to 0.01	1^{st} year fast ice
Geilfus et al. (2013)	04/09, Alaska	0.05 to 0.11 (0.077)	new fast ice
Geilfus et al. (2014)	06/12, Resolute Passage CA	-0.062 to -5*10^{-4}	1^{st} year fast ice
Nomura et al. (2010)	02/08-03/08, Sea of Okhotsk, Japan	-0.68 to 0.19	1^{st} year fast ice (Saroma-ko lagoon)
Nomura et al. (2013)	05/11, Svalbard and 01/10, Antarctica	-0.05 to 0.006	Flooded sea ice